Final Technical Report
USGS Award G11AP20127

Implementation and Application of Inelastic Soil Models in Full 3D Earthquake Simulations

Doriam Restrepo, Haydar Karaoglu,
Ricardo Taborda and Jacobo Bielak

PI: Jacobo Bielak
Computational Seismology Laboratory
Department of Civil and Environmental Engineering
Carnegie Mellon University
Pittsburgh, PA 15213-3890

Office: 123H Porter Hall
P: 412-268-2958 F: 412-268-7813
Email: jbielak@cmu.edu

July 25, 2012

Abstract

The importance of inelastic soil behavior on ground motion during strong earthquakes has been increasingly recognized in recent years. These effects are now customarily incorporated into the analysis of ground motion through one-dimensional nonlinear soil models subjected to vertically incident seismic waves. Despite the progress to date, three-dimensional (3D) effects of soil nonlinearity on the spatial and temporal distribution of ground shaking are still far from being well understood. The main objective of this project was to incorporate nonlinear soil behavior into Hercules, our finite element tool for modeling ground motion in large basins, and to demonstrate the new implementation, for studying the earthquake ground motion in the San Fernando Valley, an area that exhibited significant nonlinear soil behavior during the 1994 Northridge earthquake.

In an earlier USGS-supported project, we incorporated two material models (von Mises and Drucker-Prager) into Hercules, and used the von Mises model to simulate earthquake ground motion in a small basin. The results served to highlight the significance of the inelastic soil behavior. However, we also discovered that our implementation increased by a factor of ten the computational cost of each simulation with respect to that of the corresponding linear simulation. In this project, we have reformulated completely the theory and our computer implementation, with the result that Hercules is now able to perform simulations with both the von Mises and the Drucker-Prager models at essentially the same cost as a linear simulation. We have used the new Hercules implementation to perform a set of full 3D simulations of the 1994 Mw 6.7 Northridge earthquake, for the three material models considered. The linear velocity model used in the simulations was constructed from a discrete (etree) version of the SCECs Community Velocity Model (CVM-S, version 4.0), tailor-built to satisfy a minimum shear wave velocity of 200 m/s and a maximum simulation frequency of 2 Hz. Our results are qualitatively consistent with observations from past earthquakes. They indicate that nonlinear soil behavior affects significantly the spatial variability of the ground motion, causes permanent displacements, and reduces peak ground velocities and accelerations by a factor of up to one half. They also indicate that nonlinearity is influenced by 3D effects that cannot be represented by alternative hybrid or pseudo-nonlinear approaches commonly used in seismic hazard analyses.

As part of this project, we also explored the possibility of including the effects of pore pressure for small deformations in order to eventually estimate incipient liquefaction. To this end, we introduced into Hercules a mixed elastodynamic formulation that uses displacements and pressure as the primary field variables, and verified, through examples, that this formulation is capable of representing the full range of behavior, from a solid to an acoustic medium. This is discussed in detail in the second part of this report. With these capabilities in place, we are ready to adopt Biots poroelastic theory into Hercules and combine it with nonlinear elastoplastic models, in order to include the effects of pore pressure in future simulations.

Part I

Implementation of inelastic material models in Hercules with an application to the 1994 Northridge earthquake

1. Introduction

A significant amount of theoretical as well as experimental data have largely demonstrated the important role that local site conditions play over the seismic ground motion registered at a specific location. Initially related mainly to conditions associated directly to soil characteristics e.g., resonance of the shallow layers, soil liquefaction, attenuation of high frequencies, etc., soil nonlinear effects have gained increased interest on their own due to the evident changes in ground motions and damage patterns recorded after moderate to strong ground shaking in seismic-prone areas and the inability for linking those outcomes to conventional local-site effects. In addition, when compared with classical concepts of linear elasticity, nonlinear material theory appears to be the natural step forward towards a much better numerical representation of the complex nature of soil deposits.

Early research in nonlinear earthquake response dates back to the lates 60's where most of the work was devoted to horizontally layered systems under vertically incident waves by one-dimensional (1D) equivalent linear methods (Idriss and Seed, 1968). 1D Equivalent linear methods compute the nonlinear response by means of linear iterative methods. Based upon the idea that a horizontally layered half-space can be treated as a conventional lumped-mass system, the goal is to determine the values of the shear modulus μ and the equivalent damping ratio ξ consistent with the level of strain induced in each layer (Kramer, 1996). Initial values for the iteration procedure and convergence criteria are usually determined in accordance with the so called stress-strain backbone curves or modulus reduction curves. Despite the apparent accuracy and satisfactory results, the method is incapable of representing the actual change in soil stiffness that occurs during the ground motion (Kramer, 1996) as well as the permanent deformations present at the end of the earthquake event. Nevertheless, the simplicity of the approach and the fact that the parameters in the stress-strain curves can be determined from experimental results have made the method to be widely accepted.

The first attempts to improve the nonlinear characterization of soils date back to the mid-1970s. Joyner (1975) and Joyner and Chen (1975), using the rheological material model proposed by Iwan (1967), did a comprehensive analysis and studied the nonlinear seismic response of two-dimensional 2D soil configurations and confirmed the importance of nonlinear behavior on site response. Other 2D studies have also helped corroborate observations and quantify the potential effects of nonlinear soil effects (Marsh et al., 1995; Elgamal, 1991; Zhang et al., 2008). Three-dimensional simulations on the other hand, have not been performed so actively as their 2D counterparts. To our knowledge, due to the computational complexity involved in the incorporation of full 3D nonlinear soil behavior in earthquake simulations, the number of nonlinear studies at a regional scale is still limited (Xu et al., 2003; Taborda, 2010; Taborda and Bielak, 2011; Restrepo et al., 2011; Fabrice et al., 2010).

For general situations, the ideas behind equivalent linear strategies are no longer useful and cannot be easily extrapolated to multidimensional conditions. For instance, it is not possible to find an analogous representation for the backbone curves for general three-dimensional (3D) situations. As a result, researchers have resorted to classical theory of plasticity to meet such challenges. Originally formulated for metals, plasticity theory concepts have been successfully used in geotechnical problems in such a way that, currently, plasticity theory of geomaterials as a new field, has reached a very wide scope and significant scientific credibility as a consistent framework for the prediction of soil behavior.

Plasticity in geomaterials adopts the basic elements of flow plasticity theory: existence of an initial *yield surface* or *yielding criterion* , evolution of subsequent loading surfaces *hardening rule*, and the existence of an appropriate *flow rule* (Chen and Mizuno, 1990). The definition of the onset of plasticity is governed by the *yielding criterion*. Certainly, the best known yielding model for soils is the Coulomb's failure criterion, an irregular hexagonal pyramid in the principal stress space. Even when the Coulomb criterion is generally simple, and depends on physical parameters readily obtained from conventional laboratory results, it gives rise to numerical difficulties regarding the plastic flow at the corners of the yielding surface. Drucker and Prager (Drucker and Prager, 1952) aimed at representing a more appealing model computational-wise, and presented a smooth function that approximates the Coulomb model. In the Drucker-Prager model, the yielding surface is expressed in terms of the first invariant of the stress tensor I_1, the second invariant of the deviatoric stress tensor J_2 and two material constants α and k. The advantages and limitations of the Drucker-Prager model can be seen in (Chen and Mizuno, 1990). Flow rules are usually expressed in accordance with associative or non-associative concepts. In associative rules, the plastic flow potential function shares the same definition as the yield surface function, in non-associative rules on the other hand, the flow rule and yielding functions differ. Although the use of associative flow rules may appear as a simple convenient mathematical device, there are much more profound mathematical reasons for its usage. For instance, it ensures well-posed boundary value problems, uniqueness of the solution and preserves the validity of the so called stability postulates (Chen and Mizuno, 1990; Yu, 2006).

In this work, we present initial results from a set of full three-dimensional (3D) simulations that incorporate nonlinear soil behaviour in the soft-soil deposits ($V_s \leq$ 500 m/s) in the greater Los Angeles basin using the main shock of 1994 Northridge earthquake for frequencies up to 2 Hz in a domain size of 85 km $\times$ 85 km $\times$ 42.5 km. Simulations are performed using Hercules, the finite-element octree-based parallel earthquake simulator developed by the Quake Group at Carnegie Mellon University. We incorporated in Hercules a rate-independent approach to simulate the nonlinear behaviour of soil materials using the Drucker-Prager failure model with associated flow rule plus isotropic linear hardening rule. A rate-independent approach combined with a backward-implicit integration scheme for the material update algorithm at the local level, appears to be highly efficient computational-wise when compared with other types of material nonlinearity.

We recognize the idealized nature of the Drucker-Prager constitutive model and all the possible caveats inherent to it for representing realistic geotechnical environments. We also recognize that even more modern and elaborated constitutive models are no guarantee for predicting the real behaviour of soils under dynamic loading or to fully recover all the physical characteristics seen from laboratory tests. This study can be seen as a natural step towards a better *qualitative* understanding of the effects which soil deposits that exhibit a mechanical behaviour different from the highly idealized linear elastic characterization have over the ground motion registered in highly populated regions.

2. Methodology

The equations of motion for a continuous body are governed by the laws of balance of linear momentum and angular momentum. In component form, the equations of motion for small displacements, take the form given by (1) where σ_{ij}, ρ and b_i are the Cauchy's stress tensor, material density and the ith component of the body forces vector respectively. Traditionally, a discrete version of (1) can be achieved by means of conventional weak formulation strategies after considering that the computational domain Ω can be discretized into non-overlapping regions Ω_e in which, over each sub-domain, the displacement field is represented by the matrix of shape functions $\mathbf{N}_e(\mathbf{x})$, and the vector of physical displacements $\mathbf{u}_e(\mathbf{t})$ at the nodes of the element (2).

$$\sigma_{ij,j} + b_i = \rho \ddot{u}_i \tag{1}$$

$$\mathbf{u}(\mathbf{x}, \mathbf{t}) = \mathbf{N}_e(\mathbf{x})\mathbf{u}_e(\mathbf{t}) \tag{2}$$

Such approximation leads to a system of ordinary differential equations (ODEs) (3), where $\mathbf{M}$ and $\mathbf{K}$ denote mass and stiffness matrices of the system assembled from the elemental matrices $\mathbf{k}^e$, $\mathbf{m}^e$ (4), $\mathbf{f}$ is the vector of equivalent body forces representing e.g., seismic sources, and $\mathbf{u}$ is the nodal vector of total displacements. (Material intrinsic damping and absorbing boundaries can easily be taken into consideration, although they were not included in these expressions for convenience).

$$\mathbf{M}\ddot{\mathbf{u}} + \mathbf{K}\mathbf{u} = \mathbf{f} \tag{3}$$

$$\mathbf{K} = \sum_e \mathbf{k}^e \quad \mathbf{M} = \sum_e \mathbf{m}^e \tag{4}$$

Equation (1) does not depend on the type of constitutive model chosen; therefore, it is still valid under nonlinear material behavior. Its discrete representation (3), however, must be re-arranged because in general, it is not possible to guarantee any longer constant elemental stiffness matrices $\mathbf{k}^e$ during the whole dynamic process. Keeping in mind that under classical plastic theory the yield condition and the flow rule are formulated in stress space i.e., *stress space formulation* (Simo and Hughes, 1998), one can easily show that after keeping the stresses as the main variables, equation (3) takes the form given in (5). Here, $\mathbf{B}$ is the matrix differential operator and σ represents the current stress state inside the sub-region Ω_e.

$$\mathbf{M}\ddot{\mathbf{u}} + \sum_{\mathbf{e}} \int_{\mathbf{\Omega_e}} \mathbf{B}^{\intercal} \sigma \, \mathrm{d}\mathbf{\Omega_e} = \mathbf{f} \tag{5}$$

The nonlinear nature of (5) forces the problem to be solved incrementally. The main goal is to find the set of updated global displacements and updated strain and stress variables such that: a) equation (5) is satisfied at each time-step $\triangle$t, i.e., the global equilibrium equation must be satisfied all the time, and b) the specified equations for the constitutive model hold at specified discrete points in Ω, i.e, material update.

Global time-stepping algorithms and material update schemes are usually divided into two well-known integrative schemes i.e., explicit and implicit integration methods. At a global scale, we followed an explicit time-marching scheme in which only previous known values of the displacements, velocities and external loads are required for the computation of similar quantities at a subsequent time step. In addition, our explicit integration scheme avoids the need for solving the coupled system of equations after considering $\mathbf{M}$ lumped. Writing down explicitly the expression for the displacements of the node i corresponding to the

next time-step $\mathbf{u}^i_{t+1}$ one obtains:

$$\mathbf{u}^i_{t+1} = \frac{\triangle t^2}{m^i}\mathbf{f}^i_t + \left(2\mathbf{u}^i_t - \mathbf{u}^i_{t-1}\right) - \frac{\triangle t^2}{m^i}\sum_e \int_{\Omega_e} \left(\mathbf{B}^\intercal \sigma\right)^i_t \, \mathrm{d}\Omega_e \tag{6}$$

In (6) and thereafter, quantities at the current time step are defined with the subindex t, while those before and after the current time with subindexes $t-1$ and $t+1$ respectively. With this in mind, $\mathbf{f}^i_t$ and m^i correspond to the current force vector and associated lumped-mass value of the node i. The summation in the right-hand side of (6) keeps the coupling between neighbouring nodes by running over all the elements associated with the node i.

At the element level, we implemented a backward-implicit integration method for the updating procedure of the internal strain and stress variables at each Gauss point of the element. Keeping in mind that under implicit schemes, updated unknown variables are expressed in terms of updated quantities that also need to be determined, iterative Newton-Raphson-like procedures are usually required. However, in the following, it will be shown that for the constitutive model chosen, no iterative strategies are needed, therefore, the updated values of the internal variables are obtained directly. This approach makes this particular failure criterion extremely convenient computationally.

2.1. Drucker-Prager Material model with Isotropic Linear Hardening - Material Update

Under classical plasticity theory postulates, it is customary to assume valid the additive decomposition of the strain tensor, in which the total strain ϵ_{ij} can be divided into an elastic and plastic part denoted by ϵ^e_{ij} and ϵ^p_{ij} respectively according to (7).

$$\epsilon_{ij} = \epsilon^e_{ij} + \epsilon^p_{ij} \tag{7}$$

It is also assumed that an admissible elastic stress field (8) where D_{ijkl} is the elastic stiffness tensor, exists, and is limited by a potential function $F(\sigma_{ij}, \mathbf{A})$ in such a way that any admissible stress must satisfy the constraint (9), i.e., an elastic stress exist only for stress states inside F.

$$\sigma_{ij} = D_{ijkl}\epsilon^e_{kl} \tag{8}$$

$$F(\sigma_{ij}, \mathbf{A}) < 0 \tag{9}$$

In (9) $\mathbf{A}$ represents hardening parameters that for general situations can be high-order tensors. In this work, however, the hardening parameters will be represented by scalar functions in terms of material constants and the equivalent plastic strain e_p, (10).

$$F(\sigma_{ij}, e_p) \tag{10}$$

The yield function and the onset of plasticity on the other hand, are determined by $F(\sigma_{ij}, e_p) = 0$. This implies that under increasing loading and plastic behavior, the stress state must stay on the failure surface, although the yield surface can change in shape and position according with variations of e_p. For a Drucker-Prager failure criterion with isotropic linear hardening rule, the yield function takes the well-known expression in terms of the second invariant of the deviatoric stress tensor J_2, the first invariant of the stress tensor I_1,

and the material constant α. The hardening rule is defined by the cohesive strength function $H(e_p)$ (12), where s and k are positive material constants. The equivalent plastic strain rate $\dot{e}_p$ is represented by (14).

$$F = \sqrt{J_2} + \alpha I_1 - H(e_p) = 0 \tag{11}$$

$$H(e_p) = k + se_p \tag{12}$$

Like the yield function F, one assumes the existence of a potential function $g(\sigma_{ij}, e_p)$ that defines the plastic flow $\dot{\epsilon}^p_{ij}$ as:

$$\dot{\epsilon}^p_{ij} = \dot{\lambda}\frac{\partial g}{\partial \sigma_{ij}} \tag{13}$$

$$\dot{e}_p = \sqrt{\dot{\epsilon}^p_{ij}\dot{\epsilon}^p_{ij}} \tag{14}$$

According to (13), the rate of plastic strain deformation is in the same direction as the gradient of g, while the plastic multiplier $\dot{\lambda}$ sets its magnitude. We assume g as in (15). By making the material constant $\beta \neq \alpha$ in (15), we are implicitly assuming a non-associative flow rule. This is done merely to keep generality in our future expressions, although as it was mentioned before, we will adopt an associative rule for our simulations i.e., $\beta = \alpha$ in order to assure uniqueness in our results.

$$g = \sqrt{J_2} + \beta I_1 \tag{15}$$

Although we previously mentioned the conditions for an admissible stress state, a broader set of rules regarding criteria for the loading-unloading conditions and constraints between the plastic multiplier and the stress state still need to be addressed. These are frequently known as the *Kunh-Tucker* complementary conditions and the *consistency* condition. The *Kunh-Tucker* conditions specify the rules for admissible stress states and the fact that nonzero plastic strain rate can take place only on the yield surface (16). The *consistency* conditions on the other hand, determines that during yield, the stress point must always remain on the yield surface (17).

$$F(\sigma_{ij}, e_p) \leq 0, \quad \dot{\lambda} \geq 0, \quad \dot{\lambda}F(\sigma_{ij}, e_p) = 0 \tag{16}$$

$$\dot{\lambda}\dot{F}(\sigma_{ij}, e_p) = 0 \quad (\text{if} \;\; F(\sigma_{ij}, e_p) = 0) \tag{17}$$

Equations (7) to (17) comprise the fundamental equations in the general theory of plasticity. These equations are complete in the sense that no other expressions are needed to represent the plastic state at a specific location inside the body, although suitable modifications must be done for computational purposes.

As previously mentioned, our problem is local in nature and can be stated as follows (Simo and Hughes, 1998): Assuming that all the local state variables (18) at point x are completely defined at the current time, and therefore the stress state is also known (19), suppose that the total strain *experiences* an increment $\epsilon_{ij_{t+1}}$ which drives the state to time $t+1$, the problem to address is to update the local variables in (18) in a manner consistent with the constitutive model in (7) to (15).

$$\epsilon_{ij_t}, e_{p_t}, \epsilon^p_{ij_t} \tag{18}$$

$$\sigma_{ij_t} = D_{ijkl}\left(\epsilon_{ij_t} - \epsilon^p_{ij_t}\right) \tag{19}$$

In the following, we will focus on the framework needed for the implementation of the Backward Euler material update algorithm. In our derivations, we will leave out subindexes $t+1$ in all our updated variables, that is, quantities with no time subindex refer to the same quantities at $t = t + 1$.

Writing down explicitly the updated elastic stress tensor in terms of the bulk modulus κ, the shear modulus μ, and the deviatoric elastic stress tensor σ_{ij_d}, (8) becomes (20). Here ϵ_{ij_d} is the total strain deviatoric strain tensor and δ_{ij} the Kronecker delta.

$$\sigma_{ij} = \kappa \epsilon^e_{kk} \delta_{ij} + \sigma_{ij_d} \tag{20}$$

$$\sigma_{ij_d} = 2\mu \left(\epsilon_{ij_d} - \epsilon^p_{ij_d} \right) \tag{21}$$

Doing the same with (13) and (14) yields

$$\dot{\epsilon}^p_{ij} = \dot{\lambda} \left(\frac{1}{\sqrt{2}} N_{ij} + \beta \delta_{ij} \right) \tag{22}$$

$$\dot{e}_p = \dot{\lambda} \sqrt{\left(\frac{1}{2} + 3\beta^2 \right)} \tag{23}$$

In (22), N_{ij} is the deviatoric unitary tensor defined as:

$$N_{ij} = \frac{\sigma_{ij_d}}{\sqrt{\sigma_{mn_d} \sigma_{mn_d}}} \tag{24}$$

Following one-parameter class integration algorithms (Simo and Hughes, 1998), equations (22) and (23) become

$$\epsilon^p_{ij} = \epsilon^p_{ij_t} + \triangle\lambda \left(\frac{1}{\sqrt{2}} N_{ij} + \beta \delta_{ij} \right) \tag{25}$$

$$e_p = e_{p_t} + \phi \triangle\lambda; \quad \phi = \sqrt{\left(\frac{1}{2} + 3\beta^2 \right)} \tag{26}$$

$$\triangle\lambda = \dot{\lambda} \triangle t \tag{27}$$

The implicit nature of (25) and (26) it is worth mentioning. For instance in (25) the plastic strain tensor ϵ^p_{ij} at $t = t+1$ (no temporal subindex) is written down in terms of the same quantity at the current time which has a known value according with (18), plus another variable N_{ij} at $t = t + 1$ whose value is also still to be determined.

Substituting the previous equations into (21) yields

$$\begin{aligned} \sigma_{ij_d} &= 2\mu \left(\epsilon_{ij} - \epsilon^p_{ij_t} \right)_d - \sqrt{2}\mu \triangle\lambda N_{ij} \\ &= \sigma^{pr}_{ij_d} - \sqrt{2}\mu \triangle\lambda N_{ij} \end{aligned} \tag{28}$$

As can be seen, we introduced the auxiliary variable $\sigma^{pr}_{ij_d}$ known as the *predictor* deviatoric stress tensor. It has the important characteristic that it is completely defined in terms of known quantities. In the same sense, it will be useful for future calculations to define a second auxiliary *predictor* variable σ^{pr}_{kk}, which allows

us to express the trace of the stress tensor σ_{kk} as:

$$\sigma_{kk}^{pr} = 3\kappa \left(\epsilon_{kk} - \epsilon_{kk_t}^{p}\right) \tag{29}$$

$$\sigma_{kk} = \sigma_{kk}^{pr} - 9\kappa\beta\triangle\lambda \tag{30}$$

It is straightforward to see that (28) can be rearranged as:

$$\sigma_{ij_d}^{pr} = \left(1 + \frac{\mu}{\sqrt{J_2}}\triangle\lambda\right)\sigma_{ij_d} \tag{31}$$

Notice that σ_{ij_d} and $\sigma_{ij_d}^{pr}$ differ only by a scale factor, which as a result implies that the generalized direction of both tensors must be the same (32) . This remarkable result allows us to re-write (28) in terms of two known *predictor* quantities, leaving $\triangle\lambda$ as the only unknown term to be determined (33).

$$N_{ij} = N_{ij}^{pr} \tag{32}$$

$$\sigma_{ij_d} = \sigma_{ij_d}^{pr} - \sqrt{2}\mu N_{ij}^{pr}\triangle\lambda \tag{33}$$

Up until now the yield function has not entered into our derivations. If we now make use of it by substituting σ_{ij_d} and σ_{kk} from (33) and (30) into the standard definitions of J_2 and I_1, and in addition we substitute e_p from (26) into the cohesive function $H(e_p)$ from (12), the Drucker-Prager yield function (11) reduces to:

$$\sqrt{J_2^{pr}} - \mu\triangle\lambda + \alpha\left(I_1^{pr} - 9\kappa\beta\triangle\lambda\right) - k - s\left(e_t^p + \phi\triangle\lambda\right) = 0 \tag{34}$$

$$J_2^{pr} = \frac{1}{2}\sigma_{ij_d}^{pr}\sigma_{ij_d}^{pr} \tag{35}$$

$$I_1^{pr} = \sigma_{kk}^{pr} \tag{36}$$

In equation (34) the only unknown term corresponds to the plastic multiplier increment $\triangle\lambda$. This equation is a conventional linear equation in one unknown that can be solved directly. The fact that for a Drucker-Prager-type constitutive model, the material update algorithm can be reduced to a simple expression in terms of one single local state variable, makes the integration procedure a highly efficient method from a computational point of view and one of the main reasons why we adopted this particular failure criterion as our starting material model.

$$\triangle\lambda = \frac{\sqrt{J_2^{pr}} + \alpha I_1^{pr} - k - se_t^p}{\mu + 9\alpha\beta\kappa + s\phi} \tag{37}$$

Introducing the Heavyside function $\langle\cdot\rangle$ in (37) defined as: $\langle\Gamma\rangle = \Gamma$ for $\Gamma > 0$ and $\langle\Gamma\rangle = 0$ for $\Gamma \leq 0$, the material update algorithm reduces to the following single-step procedure:

Find $\triangle\lambda$ from (38), then update the state variables from (25) and (26)

$$\triangle\lambda = \frac{\langle\sqrt{J_2^{pr}} + \alpha I_1^{pr} - k - se_t^p\rangle}{\mu + 9\alpha\beta\kappa + s\phi} \tag{38}$$

$$\epsilon_{ij_{t+1}}^{p} = \epsilon_{ij_t}^{p} + \triangle\lambda\left(\frac{1}{\sqrt{2}}N_{ij}^{pr} + \beta\delta_{ij}\right) \tag{39}$$

$$e_{p_{t+1}} = e_{p_t} + \phi \triangle \lambda; \quad \phi = \sqrt{\left(\frac{1}{2} + 3\beta^2\right)} \tag{40}$$

Finally, the updates stress state can be found by

$$\sigma_{ij_{t+1}} = D_{ijkl}\left(\epsilon_{ij_{t+1}} - \epsilon^p_{ij_{t+1}}\right) \tag{41}$$

Notice that the introduction of the Heavyside function takes into consideration implicitly both *Kuhn-Tucker* conditions. According to the *Kuhn-Tucker* conditions (16), a negative value in the numerator of (38) can only exist for stress states inside the yield surface. Therefore, the predictor state is the correct updated state and as a result $\triangle\lambda$ must be equal to 0. On the other hand if the numerator of (38) is > 0 then, a plastic state exists and (37) must hold.

A rate-independent approach combined with a backward-implicit integration scheme for the material update algorithm at the local level, appears to be a highly efficient method computational-wise when compared with other types of material nonlinearity. For instance, Restrepo et al. (2011) and Taborda (2010) reported a time step 10 times smaller than that required for a linear system in order to ensure the so-called *CFL* stability condition when considered the soil as a visco-plastic Perzyna-type material (Perzyna, 1963), and rate-dependant plasticity. They reported also a series of special treatments over the elements at and near the kinematic source in order to ensure numerical stability. In our new approach on the other hand, the *CFL* condition is of the same order as for elastodynamics, and no especial treatment is needed in any region of the domain. This reduces dramatically the use of computer time and other computational resources.

2.2. Apex Zone

Now, from (33) and (30) it follows that any predictor stress $\sigma^{pr}_{ij_d}$ outside the elastic zone is mapped back onto the yielding surface following a straight line of slope:

$$\tan(\psi) = \frac{\mu}{9\kappa\beta} \tag{42}$$

As a result, the straight line that crosses the I_1 axis at the apex of the Drucker-Prager failure criterion and has a slope given by (42), divides the region where the stress predictor may lie into two distinct regions (Bićanić and Pearce, 1996; Anandarajah, 2010): a *Regular zone* where the plastic potential is defined for both the predictor and the final stress state, and, therefore, the updated local variables can be found from (38) to (41), and an *Apex zone* ($\xi < \psi$) where a normal tensor to the yielding function does not exist unequivocally and any trial stress must be returned to the apex Fig. 1.

For mapping back the trial stress onto the yielding surface, we recognize that the second invariant vanishes at the apex i.e. $\sqrt{J_2} = 0$, therefore, the updated stress tensor must necessarily be a hydrostatic tensor which is fully described in terms of its first invariant. The particular form of the updated stress state (43) can easily be found after solving the reduced form of (37) as in (44).

$$\sigma_{ij_{t+1}} = p_o\delta_{ij}; \; p_o = \frac{(I_1^{pr} - 9\kappa\beta\triangle\lambda)}{3} \tag{43}$$

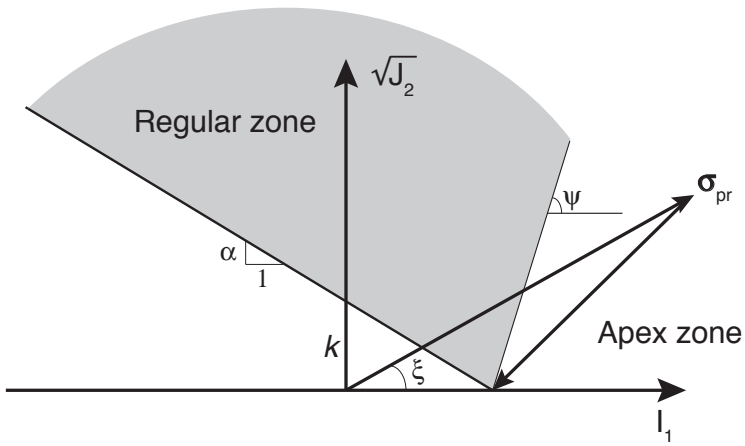

Figure 1: Regular and Apex zones in the meridional plane for a Drucker-Prager yield criterion with zero hardening coefficient s

$$\triangle\lambda = \frac{\alpha I_1^{pr} - k - s e_t^p}{9\alpha\beta\kappa + s\phi} \tag{44}$$

Notice that for the particular case where $s = 0$ i.e. zero hardening modulus, the pressure value in (43) reduces to the maximum positive pressure allowed by the failure criterion $p_o = \frac{k}{\alpha}$.

Finally, making use one more time of (43) and the strain decomposition assumption (7), it is easy to show that the updated plastic strain is given by

$$\epsilon^p_{ij_{t+1}} = \epsilon_{ij_{t+1}} - \frac{p_o}{3\kappa}\delta_{ij} \tag{45}$$

3. Numerical Results

We now focus on presenting results from a set of full three-dimensional (3D) simulations that incorporate the previously mentioned nonlinear constitutive model in the soft-soil deposits of our targeted domain. Our simulations are performed using Hercules, the finite element octree-based parallel earthquake simulator developed by the Quake Group at Carnegie Mellon University.

3.1. Region of Interest and Earthquake Scenario

The selected domain covers a volume of the crustal structure in the Southern California region of size 81.9 km $\times$ 81.9 km $\times$ 40.9 km that includes the main urban metropolitan areas in the Great Los Angeles Basin Fig. 2. Topography is not explicitly considered in our numerical domain, we follow instead a traditional approach and make topography and bathymetry a flat top surface by squashing the surface of the earth — this method usually preserves the shallow velocity gradients of the superficial layers although distort the geometry of the internal geologic structures (Aagaard et al., 2008). The internal velocity gradient was taken from the SCECs Comunity Velocity Model (CVM-S, version 4.0) tailor-built to satisfy a minimum shear velocity of 200 m/s and a maximum frequency of $f_{\max} = 2$ Hz. A fence diagram extracted from Version 2 of the SCEC 3D seismic velocity model of southern California showing S-wave velocity variations along the most important basins

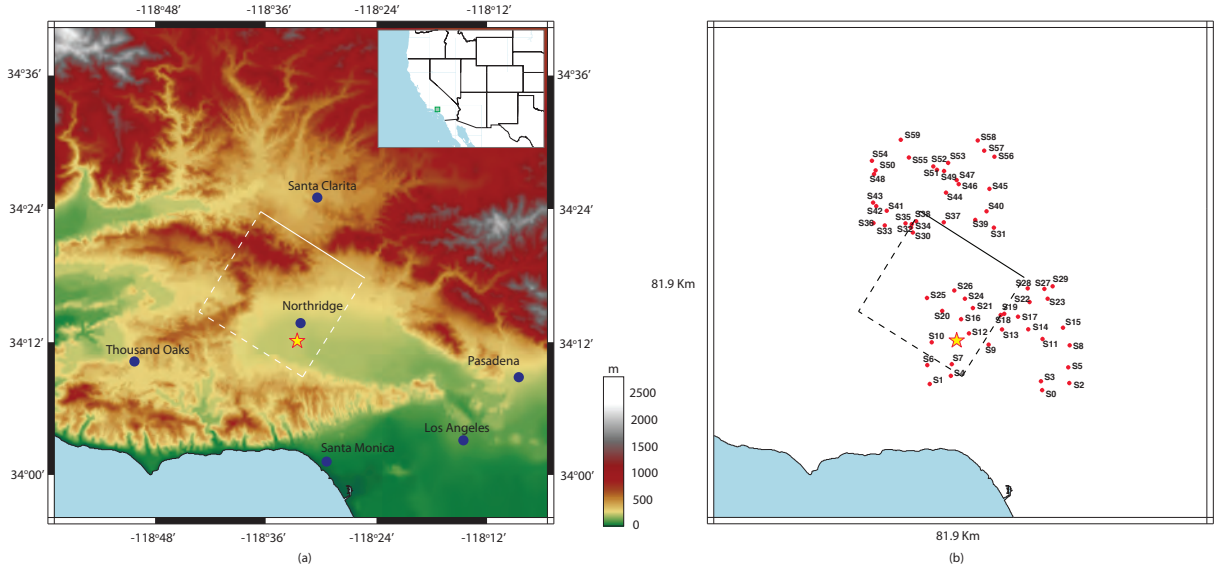

Figure 2: Region of interest. (a) Elevation model of the region of interest. (b) Location of of stations. Continuous line and dotted lines depict the direction along strike of the fault plane and its projection on the free-surface. Yellow star shows the epicenter of the 1994 Northridge earthquake. Snippet at the top right hand corner shows the global location of the simulated domain.

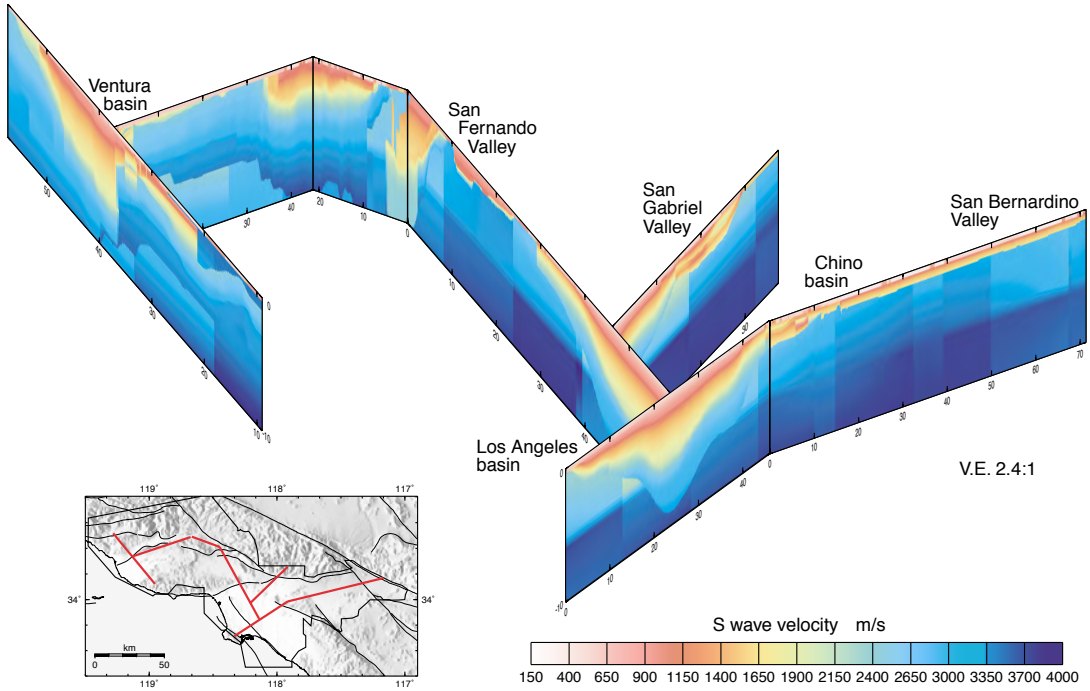

Figure 3: Fence diagram of shear wave velocities from the version 2 of the CVM (after Field and the SCEC Phase III Working Group, 2000)

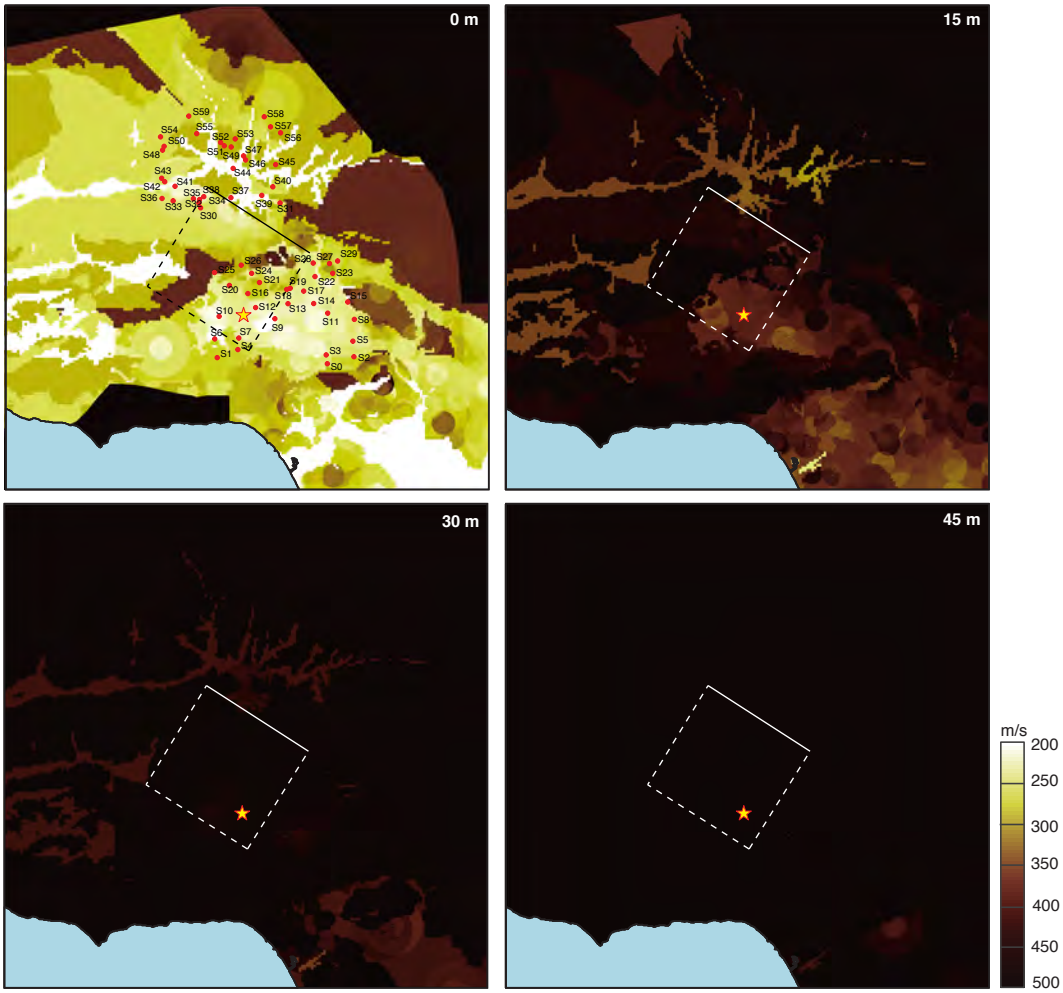

Figure 4: Shear wave velocities for $z = 0$, $z = 15$, $z = 30$ and $z = 45$ m as read from the SCEC's Comunity Velocity Model (CVM-S, version 4.0)

covered by the model is presented in Fig. 3 after Field and the SCEC Phase III Working Group (2000). A more detailed description of the internal velocity gradient is shown in Fig. 4. Here, the increasing stiffness of the shallower sedimentary deposits in the top 60m becomes evident.

We simulate the 17 January 1994 Northridge $M_{\mathrm{w}} = 6.7$ event because of the comprehensive amount of strong ground motion data produced in addition to the evidence of important nonlinear sediment response also associated with this event (Field and the SCEC Phase III Working Group, 2000), (Beresnev et al., 1998). To model the earthquake's source we used the kinematic representation of the fault rupture generated by Graves and Pitarka (2010). The fault is 20 km long and has a down-dip width of 25km. The fault plane is oriented with a strike and dip of 122°and 40°respectively, the average rake angle is 101°(Graves and Pitarka, 2010). In Fig. 2 and henceforth, the closest edge of the fault plane to the free surface is depicted with a solid line, while dashed lines represent the surface projection of the fault, the yellow star is the epicenter of the 1994 Northridge event.

3.2. Nonlinear Material Properties

To date, the number of advanced constitutive models that accurately describe the rheology of the soil at different strain levels is abundant. In some cases however, these models appear to focus on predicting the local nonlinear response by means of highly complex expressions based upon a large number of variables that cannot be easily obtained from standard laboratory tests, and under the assumption that numerical integration can be performed in an straightforward manner, even when it has been shown that they are susceptible to numerical failure (Borja and Lee, 1990).

As previously indicated, we adopted a Drucker-Prager failure criterion as the nonlinear constitutive model in our numerical simulations. The advantage of using such a model is twofold. In the first place, the integration of the constitutive model can be solved directly by means of a quite simple, yet effective returning-map class integration algorithm based upon the evaluation of just a single expression (38); second, the material variables k and α in (11) and (12) can be characterized by two soil parameters, the cohesion c and the friction angle ϕ if the the Drucker-Prager failure criterion is made to coincide either at the outer (46) or the inner edges (47) of the so-called Mohr-Coulomb model (de Souza Neto et al., 2008).

$$\alpha = \frac{2\,\sin\,\phi}{\sqrt{3}\,(3-\sin\,\phi)}, \quad k = \frac{6c\,\cos\,\phi}{\sqrt{3}\,(3-\sin\,\phi)} \tag{46}$$

$$\alpha = \frac{2\,\sin\,\phi}{\sqrt{3}\,(3+\sin\,\phi)}, \quad k = \frac{6c\,\cos\,\phi}{\sqrt{3}\,(3+\sin\,\phi)} \tag{47}$$

Despite of important advances aimed at developing a unified tool for the characterization of internal variations of soil properties in realistic domains as the SCEC CVM-S model, where the most up-to-date values of P-wave velocity V_{p}, S-wave velocity V_{s}, and density ρ can be queried at any specific location in the southern California region, these are limited to linear soil behavior. Therefore, a complete geotecnichal description in terms of c and ϕ values needed in even simple constitutive models as ours is still lacking. An indirect strategy focused on obtaining realistic cohesion values can, however, be followed as in Hartzell et al. (2004). Here, making use of the effective mean stress $\sigma_{\mathrm{m}} = (\sigma_{\mathrm{v}}/3)(1+2K_{\mathrm{o}})$, where σ_{v} and K_{o} are the vertical effective stress and the coefficient of lateral stress at rest respectively, as well as the reference strain value γ_{ref} obtained as the value of strain from the modulus reduction curves when the ratio between the shear modulus G and the maximum elastic shear modulus $G_{\mathrm{max}} = \rho {V_{\mathrm{s}}}^2$ equals 0.5, i.e., $G/G_{\mathrm{max}} = 0.5$, Hartzell et al. (2004) determined the c value for a column of soil with the same strength resistance as implied by the modulus reduction curves (48). Values for the friction angle on the other hand, have traditionally been assumed as $\phi = 30°$.

$$c = \frac{(\gamma_{\mathrm{ref}} G_{\mathrm{max}} - \sigma_{\mathrm{m}} \sin\,\phi)}{\cos\,\phi} \tag{48}$$

In this study we followed a simpler approach and made a series of approximations regarding the specification of the nonlinear parameters. In the first place, we artificially assumed that only soil deposits with V_{s} values below 500 m/s were susceptible of plastic behavior while the remaining were kept linear; second, we directly assigned values for the yielding limits k and α in (11) and (12). For the k soil parameters, we divided the assumed nonlinear range into six discrete sub-ranges: 200 - 250 m/s, 250 - 300 m/s, . . . 450 - 500 m/s., and computed over each interval the average value of the $\sqrt{J_{2_{\mathrm{avg}}}}$ term from a reference linear simulation, then, the final k values over each sub-range was set to 75% of its correspondent reference $\sqrt{J_{2_{\mathrm{avg}}}}$ value. Values for

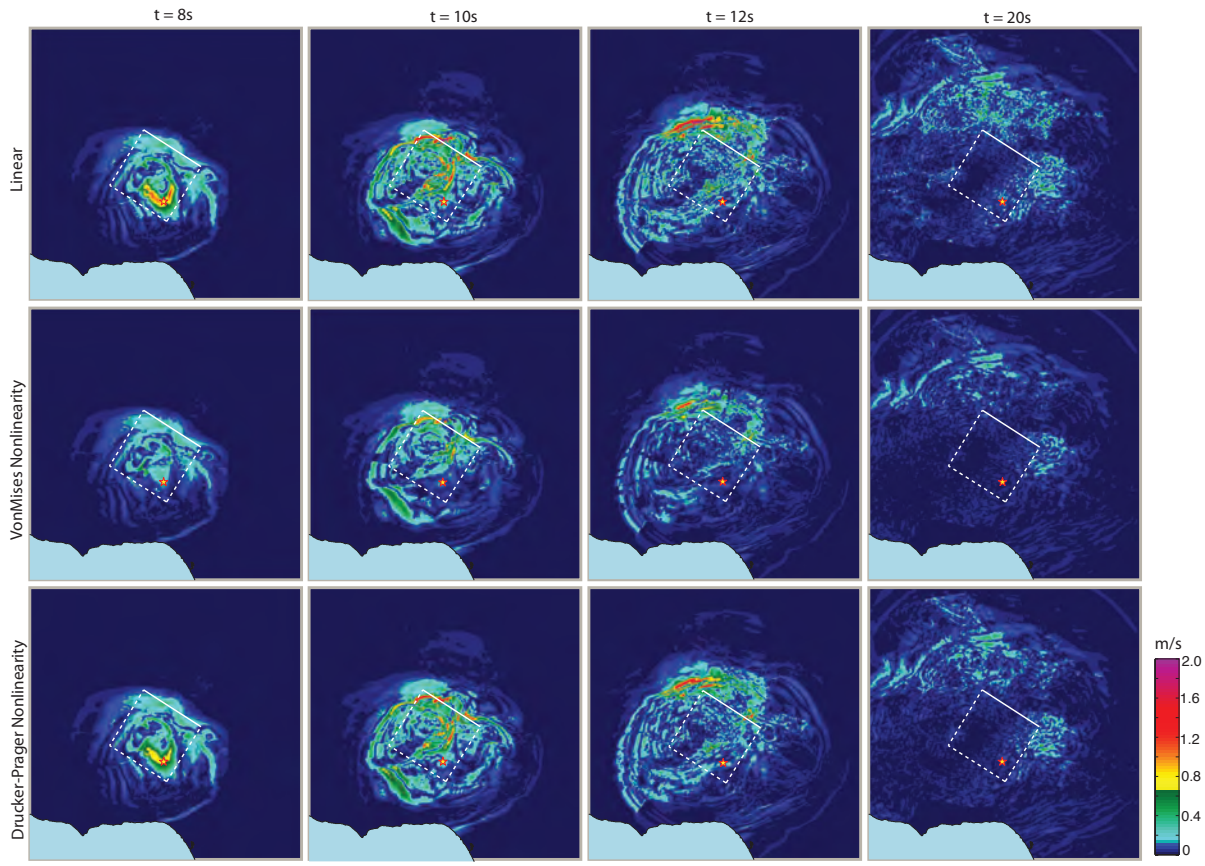

Figure 5: Snapshots of the absolute amplitude of the EW and NS components of particle ground velocity at different times for the linear (top), Von Mises (middle) and Drucker-Prager (bottom) simulations.

the parameter α were computed from (46) assuming $\phi = 30°$ and because we adopted associative plasticity, $\beta = \alpha$ in (15). Finally, we set to 0 the value of s in (12) due to lack of information regarding this parameter.

3.3. Simulation Results

As is well known, a von Mises failure criterion can easily be obtained from (11) just by setting $\alpha = 0$. Because of this, in the following, we compare results obtained from considering these two nonlinear failure criteria i.e., Drucker-Prager (DP) and von Mises (vM) with respect to the corresponding linear response.

As a starting point, we study the time evolution of the ground motion by comparing the magnitude of the horizontal surface velocities of the nonlinear cases with respect to the corresponding linear response, as shown in Fig. 5. Here, snapshots of particle ground velocity computed as the square root of the sum of the squares of the EW and NS velocity components, show that at the first stages of the rupture process (t = 8s), linear and DP results exhibit good agreement although a reduction in the DP response near to the epicenter is evident as a result of the additional dissipation from the nonlinear behavior. VM results on the other hand, present a much larger reduction, suggesting larger nonlinear effects. It is important to point out that first wavelet packets appear unaffected by the presence of nonlinear behavior as can be seen from the two

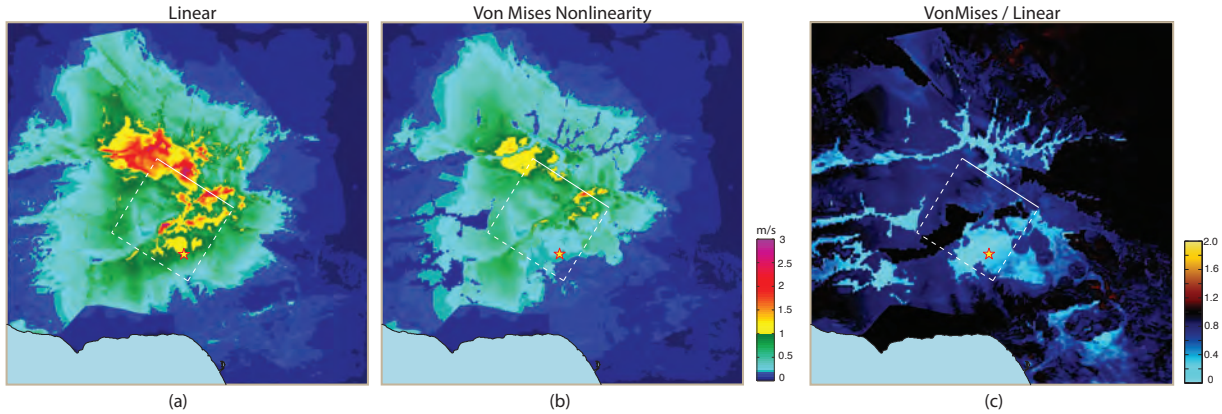

Figure 6: Peak ground velocity values computed as the maximum absolute value of the EW and NS components of particle ground velocity for the linear (a) and the Von Mises (b) simulations. Figure (c) depicts the ratio of the Von Mises results over the linear PGV values.

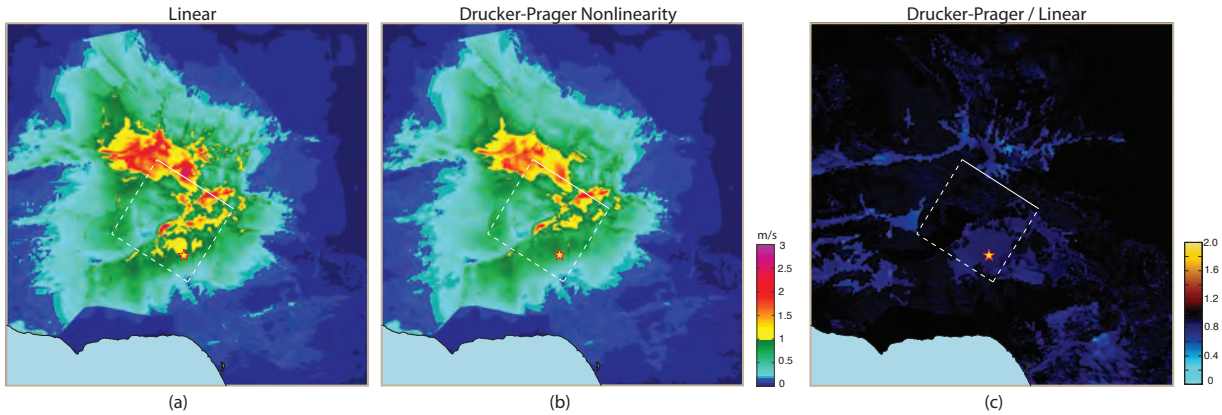

Figure 7: Peak ground velocity values computed as the maximum absolute value of the EW and NS components of particle ground velocity for the linear (a) and the Drucker-Prager (b) simulations. Figure (c) depicts the ratio of the Drucker-Prager results over the linear PGV values.

packets travelling south-east towards the Santa Monica region and south-west towards the Thousand Oaks area.

As the rupture process advances ($t = 10$ s and $t = 12$ s), the response from the soil deposits becomes more evident. Here, a clear amplification of the Thousand Oaks wavelet packet by basin local effects is shown at $t = 10$ s. Surprisingly, shape and amplitude values of the packet are almost the same magnitude for all three scenarios. As in the previous case, most of the differences between linear and nonlinear simulations are concentrated inside the projected area of the fault plane with larger reductions still associated with von Mises type nonlinearity. At $t = 12$ s a packet of waves of large energy is initiated at the north-west corner of the fault plane presenting similar magnitude values in all three simulations but, with a noticeable change in the spatial spreading, again, being larger for the linear response, minimum for the von Mises response and in between for the Drucker-Prager nonlinearity type.

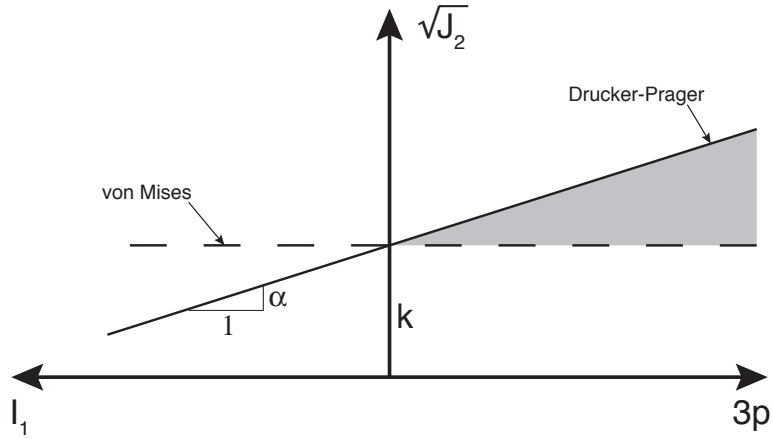

Figure 8: Shapes of the von Mises (dotted line), and Drucker-Prager (solid line) failure criteria in the meridional plane.

Late phases and basin reverberations are the common characteristics at t=20s. As in the previous cases, these are larger for the linear simulation. In all cases, two major clusters of surface waves appear to be localized at the north part of the domain and the south-east corner of the top edge of the fault plane.

3.3.1. Peak ground velocity PGV

A better evaluation of PGV variations is achieved by looking at Fig. 6 and Fig. 7. In the first, larger amplitudes are located north from the epicenter and enclosed by the fault plane projection, with the highest levels at the north-west corner of the top edge of the fault. As expected, linear simulations exhibit the larger magnitudes in PGVs. Zones of larger response from the vM simulation are also located near the top left side of the fault although distributed over a smaller area. Regions of maximum response within the interior of the projected fault plane are greatly reduced in size by the nonlinear response. Differences between PGVs values are highlighted in Fig. 6 (c) which shows the ratio between the nonlinear and the linear response. Red colors depict areas where the vM results exhibited amplification and blue colors indicate deamplification. Black on the other hand denotes no change. As can be readily seen, vM results present reductions throughout the entire domain — black and blue colors in Fig. 6 (c) — with reductions as high 0.2 times the linear response. Regions of maximum reductions concentrate around the epicenter area and following the the alluvial sediments of the Santa Clara river.

On the other hand, Ducker-Prager results exhibit a closer agreement when compared with results from the linear response Fig. 7 (a) and (b). Here, areas in blue, cyan and green depicting the far and intermediate PGVs fields are basically preserved in both simulations. The shape of the region of maxima — yellow to red colors — at the top left corner of the fault plane is also similar although a modest reduction of the DP results is evident. Ratios between responses Fig. 7 (c) on the other hand, share a fairly close resemblance with its counterpart in Fig. 6 (c). For instance, these still concentrate in the region enclosed by the projection of the fault plane near the epicenter and following the Santa Clara riverbed, although with lower reductions.

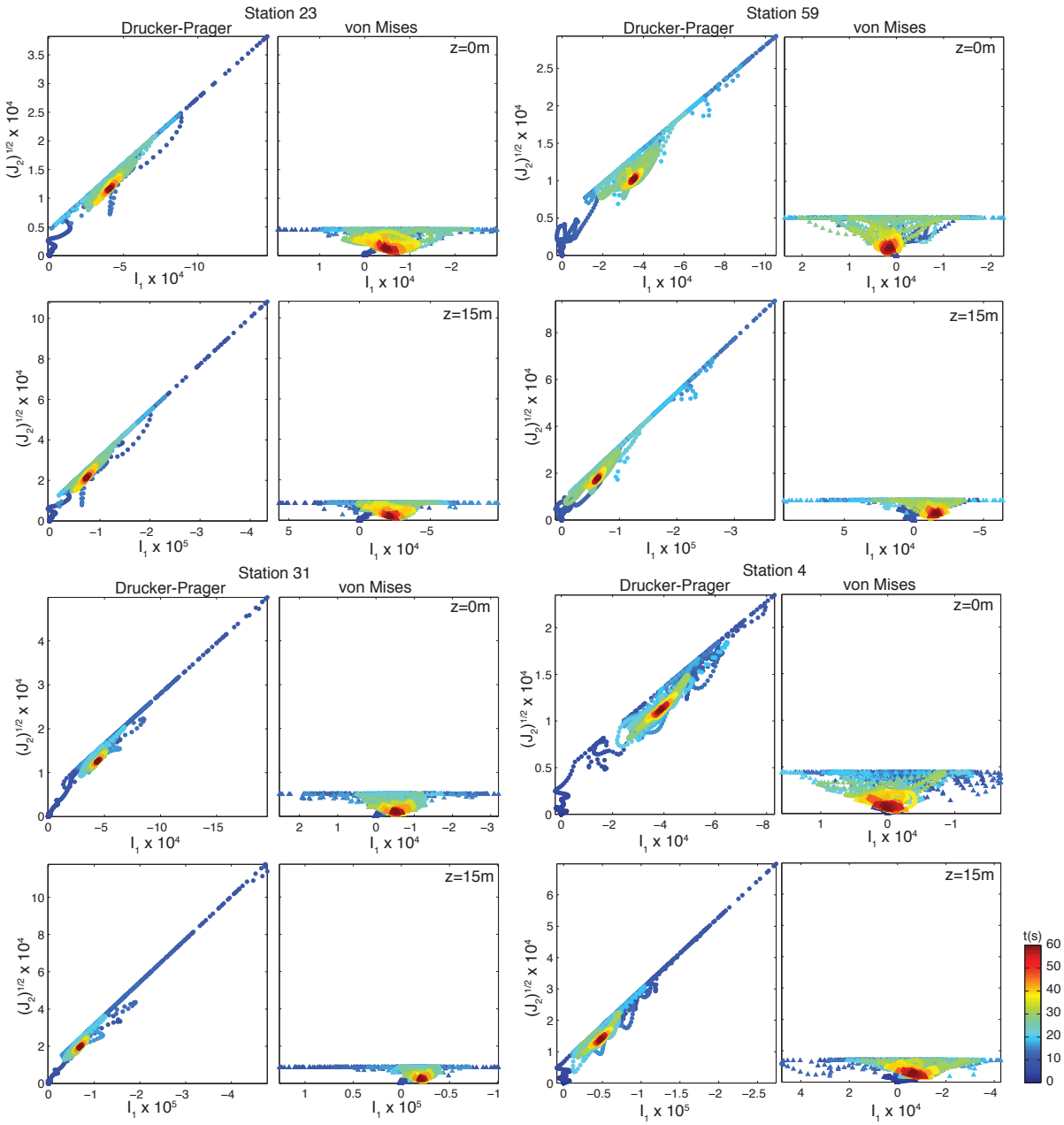

Figure 9: Plots in the $I_1 - \sqrt{J_2}$ plane for stations S4, S23, S31 and S59 at two different dephts (z=0m and z=15m) for the Drucker-Prager and von Mises nonlinear criteria. Colors represent time in seconds. Units in kgf/m^2.

A possible explanation for the linear-like behavior displayed by the DP results could be related to an increase of strength as a consequence of positive increments in the internal pressure p. As is known, a Drucker-Prager failure criterion appears as an open cone in the principal-stress space, which expands as the pressure $p = -I_1/3$ increases, while the von Mises criterion, being pressure independent, is represented by a circular cylinder. In the meridional space ($I_1 - \sqrt{J_2}$ plane) they appear as two straight lines Fig. 8. As the meridional representation shows, the gray area renders two different physical scenarios depending on the failure criterion chosen, i.e. stress states inside the gray area exhibit a nonlinear behavior according to the von Misses model and are forced to return onto the yielding surface, whereas the same stress state exhibits a linear behavior and is allowed to stay as it is if a Drucker Prager failure criterion is used instead.

Positive pressure values are more likely to occur if an initial geostatic stress state is considered. In this study, however, we did not consider any initial geostatic pressure. Therefore, only dynamic pressures were measured. Focusing at checking the evolution of pressure and therefore a possible strength gain, Fig. 9 presents plots of I_1 vs $\sqrt{J_2}$ at selected locations throughout the region of interest. The strength increase exhibited by the DP response at all stations is evident. The increase in strength for the DP model is as large as ten times the the yield level from the vM simulations. In terms of the development of nonlinearity, it appears that the onset of plasticity initiates at t=10s and extends until t=25s in almost all locations and for both nonlinear criteria. There is a residual stress for both nonlinear conditions. For the DP model the large residual stress state can be seen through the yellow-to-red points. For the vM model, permanent stresses are also visible although in a lesser amount and with a marked tendency to reach the stress condition at rest.

3.3.2. Peak Ground Acceleration PGA and Peak Ground Displacement PGD

Another set of results is shown in Figs. 10 and 11. Here, comparisons between PGA values from the nonlinear models with the linear results are presented. As expected, nonlinear results exhibit smaller values as a result of the additional amount of energy dissipation capacity given by the nonlinear behavior. As for the PGV, maxima are concentrated inside the fault's projected area and, especially, at the north-west corner of the along-strike top side of the fault. We associate these amplifications with strong rupture directivity effects produced toward the north by the 1994 Northridge earthquake (Graves and Pitarka, 2010). The linear and DP results exhibit values greater than 1g, as can be seen by the saturated scale in Fig. 11. Results from the vM criterion present maximum PGA values of just 0.7g, again, as a result of larger reductions produced by the lack of pressure dependence and the relatively low yielding limits assumed.

Permanent, or residual ground displacements RGD computed as the average value over the last 15s of simulation of the square root of the sum of the squares of the EW and NS component of particle displacements, are shown in Figs. 12 and 13. Although linear and nonlinear simulations share the same pattern, there are some differences. For instance, linear results tend to exhibit a smoother and homogeneous spatial variability, which follows the superposition of the radiation patterns from the asperities that make up the fault. By contrast, nonlinear RGD values are heterogeneous and composed by very pronounced sharp variations, particularly near to the region of maximum linear displacements which appears as the red strip shown in Fig. 13 (b). These differences are also visible in terms of the final magnitudes. Contrary to the previous cases, vM results exhibit the larger RGD values because of the larger plastic strain needed to accommodate the low yield levels assumed. Linear results on the other hand present the lower values, and DP on average shows intermediate values.

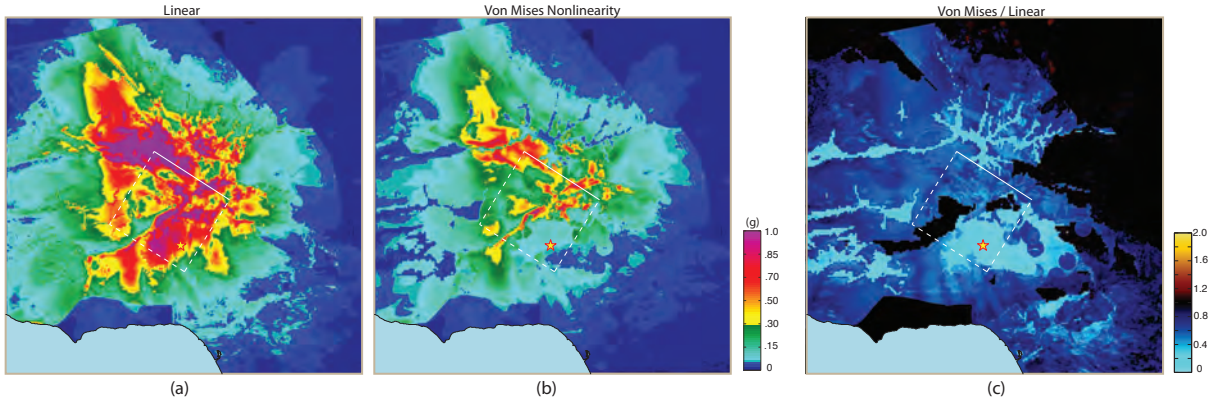

Figure 10: Peak ground acceleration values computed as the maximum absolute value of the EW and NS components of particle ground acceleration during the whole simulation time for the linear (a) and the Von Mises (b) simulations. Figure (c) depicts the ratio of the Von Mises results over the linear PGA values.

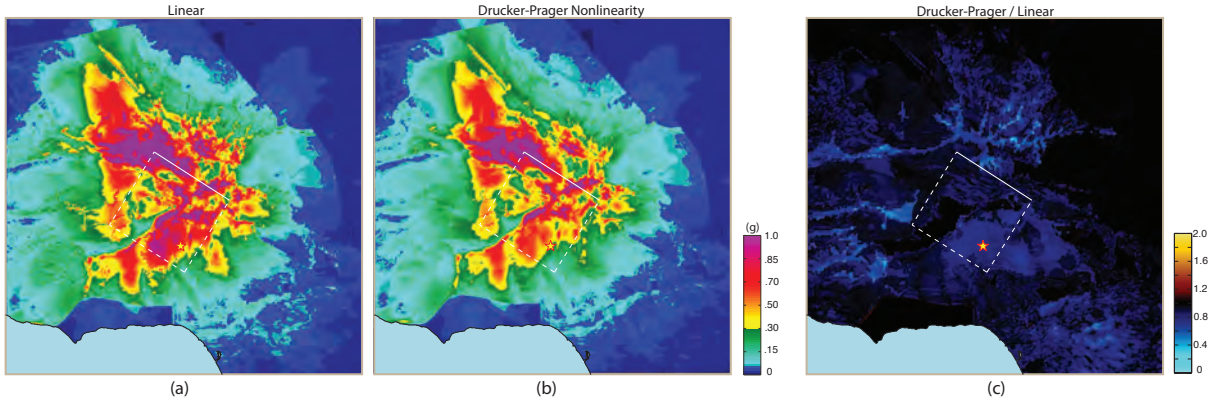

Figure 11: Peak ground acceleration values computed as the maximum absolute value of the EW and NS components of particle ground acceleration during the whole simulation time for the linear (a) and the Drucker-Prager (b) simulations. Figure (c) depicts the ratio of the Drucker-Prager results over the linear PGA values.

The discrepancies between the two cases and influence of the plastic deformation in the nonlinear cases can be appreciated in greater detail in Figs. 12 (c) and 13 (c) . Theses figures show the difference in permanent displacements (nonlinear - linear) for the corresponding model. Warm (red) indicates that the nonlinear permanent displacement was larger than the obtained under elastic soil conditions, cool (blue to cyan) indicates that the permanent displacement observed in the nonlinear simulation was smaller than its linear counterpart). For the most part, the nonlinear simulations present larger permanent displacements than the linear one. The regions where this is not the case, however, call into question the common belief that permanent plastic deformations are always expected to be larger than those from linear simulations and may be an evidence of the presence of complex 3D basin effects. No, or little, difference is observed in the near the top and to the right side of the domain.

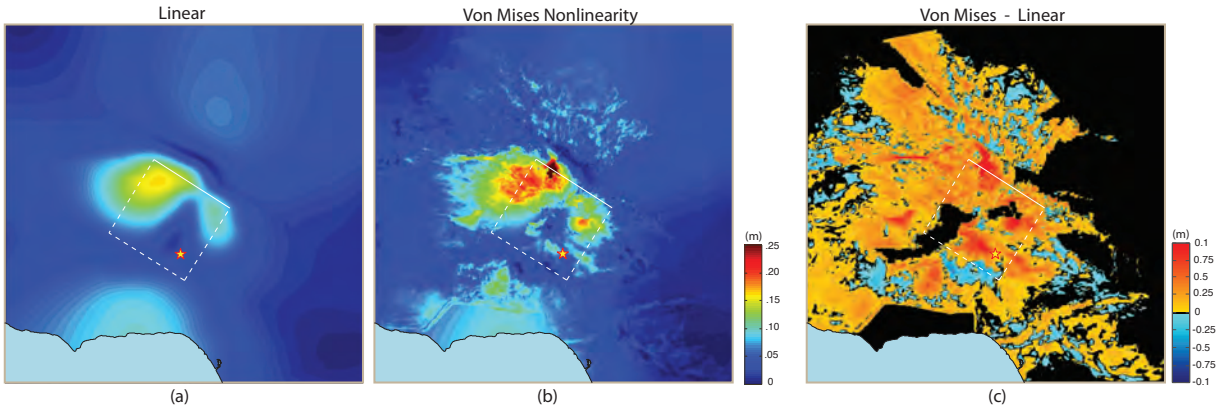

Figure 12: Rermanent displacement values computed as the average value of the maximum absolute value of the EW and NS components of particle ground displacement during the last 15 seconds of the simulation for the linear (a) and Von Mises (b) simulations. Figure (c) depicts the difference between the nonlinear and linear permanent displacements values "Nonlinear minus Linear".

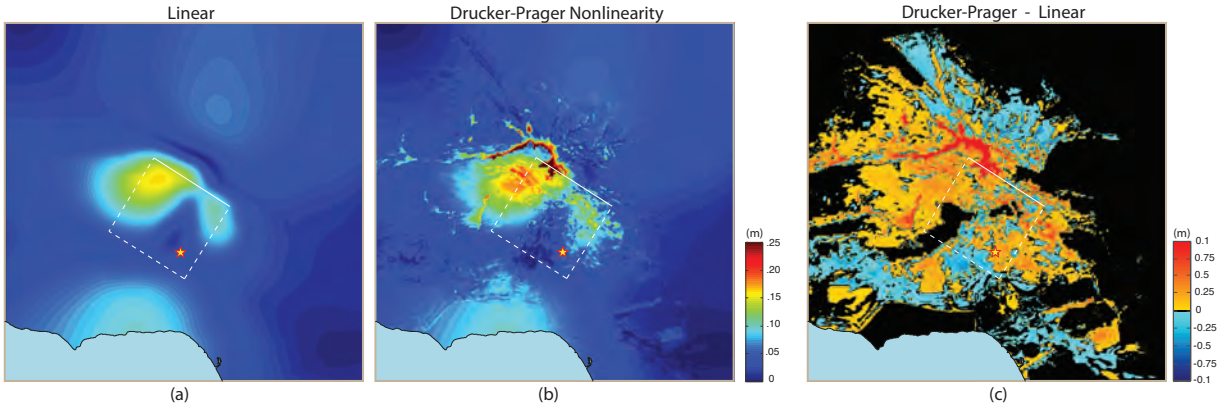

Figure 13: Rermanent displacement values computed as the average value of the maximum absolute value of the EW and NS components of particle ground displacement during the last 15 seconds of the simulation for the linear (a) and Drucker-Prager (b) simulations. Figure (c) depicts the difference between the nonlinear and linear permanent displacements values "Nonlinear minus Linear".

3.3.3. Local Respose

Figures 14 to 16 compare the synthetic waveforms at select locations throughout the region of interest. Station location are shown in Fig. 2 (b). These stations were chosen such that there would be a complete description of the nonlinear variations throughout the region.

We begin our observations by checking modifications produced by nonlinear effects over stations that are supposed to have a fault-controlled response, that is, stations where strong rupture directivity effects may be dominant. With this in mind, Fig. 14 presents ground-velocity and ground-acceleration waveforms for three near-epicenter stations: S16, S20 and S25. Station S25 presents the expected pulselike arrival with strongest response along the fault parallel component. Surprisingly, the waveform appears unaffected by any nonlinear effects in both velocity and acceleration. This situation, may be a consequence of the stiffer soil-deposits beneath station S25 rather than by directivity effects per se.

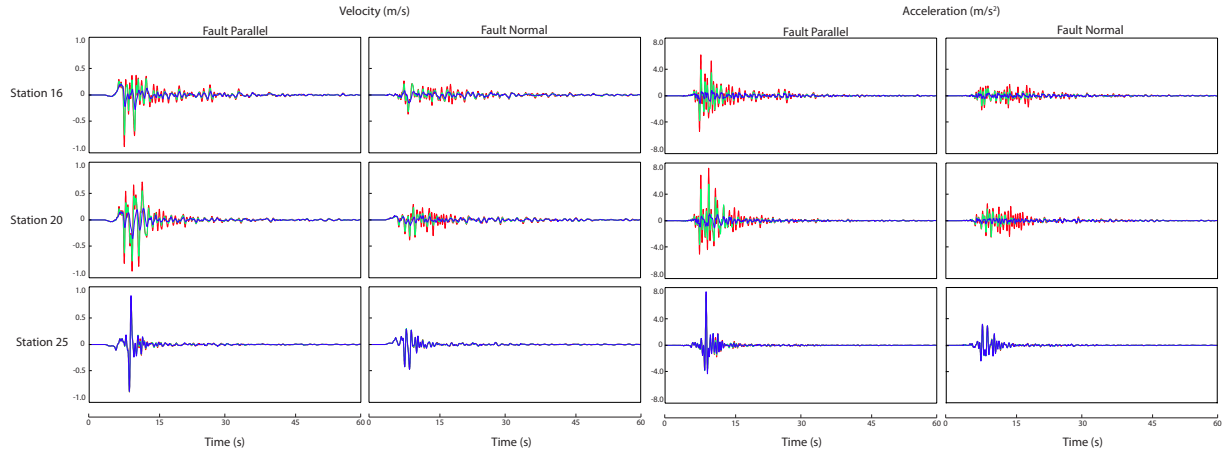

Figure 14: Simulated ground waveforms for stations: S16, S20 and S25 for the Northridge earthquake. Linear (red), Drucker-Prager (green) and von Mises (blue) lines, depict the parallel to fault (122°) and normal to fault (212°) rotated components of velocity and acceleration.

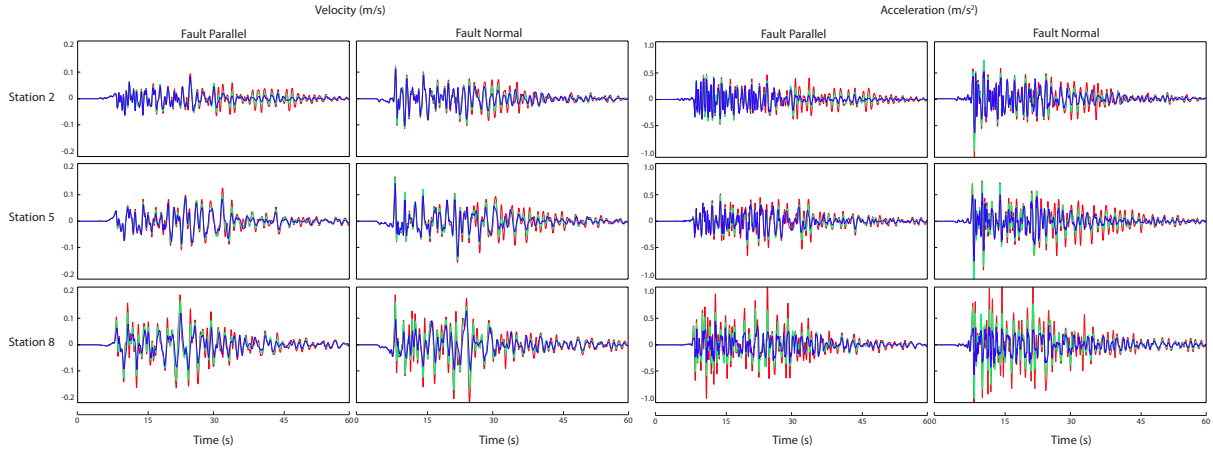

Figure 15: Simulated ground waveforms for stations: S2, S5 and S8 for the Northridge earthquake. Linear (red), Drucker-Prager (green) and von Mises (blue) lines, depict the parallel to fault (122°) and normal to fault (212°) rotated components of velocity and acceleration.

Stations S16 and S20 also present a pulselike behavior with stronger response in the parallel fault direction, although the waveforms suggest a modest interaction with the shallower soil deposits. Nonlinear effects are clearly visible (which reinforces the idea of moderate local effects). As discussed previously, the ratios between the von Mises and the linear results of velocity reach values as low as 20%.

Accelerations tend to be affected by the higher frequencies, while contributions from rupture directivity and radiation pattern dominate the low-frequency velocity waveforms (Wald et al., 1996). With this in mind, acceleration traces at stations S2, S5 and S8 Fig. 15, suggest the existence of pronounced effects from local soil conditions. Here, late phases and interaction with basin surface waves dominate the ground shaking, with larger response controlled by the fault normal component. The fault normal components of acceleration at stations S2 and S5 present a marked reduction with respect to the vM results from the early stages of the ground motion. However, results from the DP model show a similar response to that of the linear

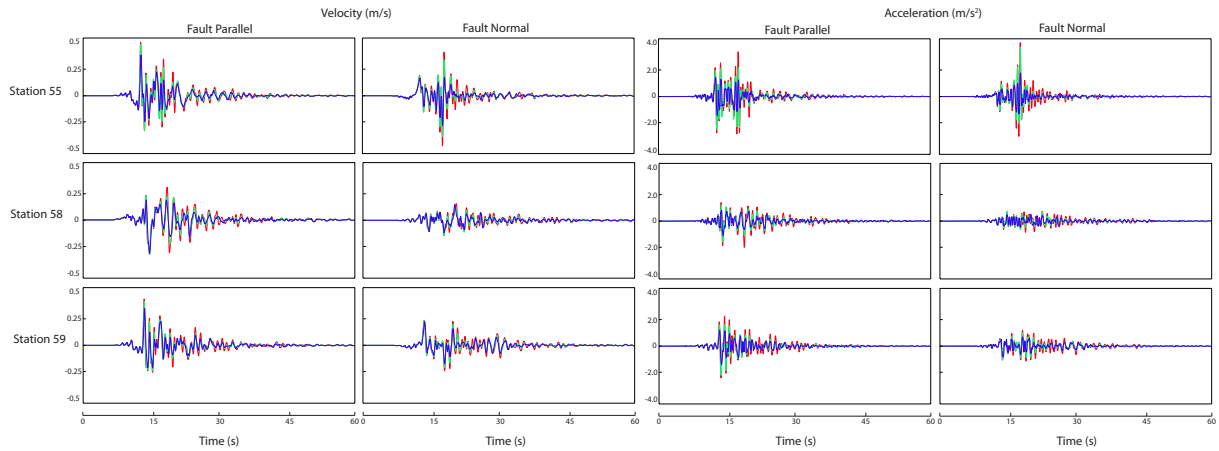

Figure 16: Simulated ground waveforms for stations: S55, S58 and S59 for the Northridge earthquake. Linear (red), Drucker-Prager (green) and von Mises (blue) lines, depict the parallel to fault (122°) and normal to fault (212°) rotated components of velocity and acceleration.

model, at least during the phase of intense ground shaking and up until 25s approximately. This suggests that at these particular stations, DP nonlinearity presents a major effect over late phases and free surface reverberations, than over the direct waves that make up the stronger early arrivals. Station S8 on the other hand, exhibits more pronounced basin effects and larger nonlinear modifications from the early stages of ground motion. This station is located in the vicinity of an area filled with hard soil deposits located at the foot of the Verdugo mountains (Glendale, CA). Although a detailed analysis is still needed, we believe that focusing effects caused by subsurface basin structure similar to those observed in Santa Monica during the 1994 Northridge earthquake (Graves et al., 1998) may be the source of important constructive interference and the cause for the strong variability in the response at S8 as well as the early nonlinear response.

The Northridge earthquake produced strong rupture directivity towards the north (Graves and Pitarka, 2010). This is noticeable from the typical near-field pulse-like shape of the synthetics of velocity of stations S55, S58 and S59 (Fig. 16). A modest interaction with the soil deposits is also perceptible. The comparison in the time domain confirms the results presented earlier regarding the reductions observed in PGV and PGA due to soil nonlinear behavior. Here, maximum von Mises over linear PGV ratios reach values of 70% in both horizontal components of station S55. PGV values for station S58, on the other hand, attain the same value for all three models. Drucker-Prager PGV results attain the same values than its linear counter part except for the fault normal component, for which a small reduction of 15% occurred.

4. Concluding Remarks

We presented numerical results for the 17 January 1994 Northridge $M_{\mathrm{w}} = 6.7$ earthquake rupture model over a volume of the crustal structure in the Southern California region of size 81.9 km $\times$ 81.9 km $\times$ 40.9 km for frequencies up to 2Hz, considering three different material models: 1) Linear anelastic, 2) pressure dependent elasto-plastic Drucker-Prager yield criterion and 3) elastic-perfectly plastic von Mises nonlinear criterion.

Nonlinear strategies showed, in general, reductions and spatial variations when compared with results from the linear reference simulation. Our numerical findings showed that the level of reduction is strongly affected by the type of constitutive model selected. Under elasto-perfectly plastic von Mises nonlinear behavior, the PGV is reduced to as much as 20% of the linear reference. However, when some level of additional resistance given by the internal pressure is considered, as in the Drucker-Prager failure criterion, those reductions reached only 80% percent of the reference linear response. This strength increment with pressure, while in agreement with the real behavior of geomaterials, does not exhibit an infinite value as the open Drucker-Prager cone indicates. This suggests that under a more realistic model, such as a Drucker-Prager-Cap criterion a larger level of nonlinear soil response would be expected.

We presented a comprehensive and fairly detailed formulation for the material update algorithm. We showed that following an implicit scheme at the local level for the integration of the evolution equations in conjunction with an explicit formulation at the global level, appears to be numerically stable, with no numerical artifacts and leading to acceptable ground motion estimates.

Nonlinear simulations greatly depend upon the flexibility of the constitutive models for incorporating meaningful and easy to obtain soil parameters. The Drucker-Prager failure criterion shares these properties and despite its relative simplicity, it can lead to reasonable agreement between results of simulations and observations for problems that do not involve soil liquefaction (Xu et al., 2003). Our initial set of results, while providing valuable knowledge on the effects of nonlinearity over seismic response, still require additional work to properly account for realistic soil properties. We believe that the Hartzell's approach presented previously is a good starting point towards fulfilling this condition.

Part II

Unified FEM for Elastic and Acoustic Media Wave Propagation

1. Introduction

The development of a unified formulation to model wave propagation in different media ranging from elastic to acoustic with a robust finite element method has been the objective of research efforts for many years. These efforts have been primarily aimed at fluid-structure interaction problems, including those encountered in many earthquake and tsunami problems.

Early works in this area include the modeling of fluids as, incompressible elastic material (Hughes, 2000, chapter 4). Remaining within the limits of linear elasticity, another path to model acoustic fluids has been to take the shear modulus as zero (Olson and Bathe, 1983). Determining the appropriate boundary and interface conditions (*slip, no-slip*) has also been the focus of attention. Discussions on this topic go back to the early twentieth century (Prandtl, 1904).

In the traditional finite element method, the governing equations are expressed in terms of displacement variables. However, the numerical results deteriorate badly as the Poisson's ratio approaches 1/2. It has also been observed that this formulation results in spurious modes (circulation modes) with non-zero frequencies (Kiefling and Feng, 1976) for acoustic problems, thus, failing to be a general one. Introducing irrotationality constraint, Hamdi et al. (1978) developed a formulation for which the frequencies of the circulation modes increase with the constraint constant introduced. This solves the problem as long as the frequency range of interest lies below the maximum frequency values of interest. However it does not mean that these modes are completely eliminated.

Another approach has been to use the displacements as variables in the solid and pressure (or velocity potentials) in the fluid (Zienkiewicz and Newton, 1969). However, these formulations include unsymmetric matrices that render them difficult for programming purposes.

Another alternative is to use mixed finite element formulations, using both displacement and pressure. This requires a stability condition generally referred to as *inf-sup condition* (Babuška, 1971; Brezzi, 1974) for eliminating the spurious modes, which puts a limit on the type of elements that can be used.

In this work, we consider a unified approach that is robust within the entire range of an elastic solid with moderate contrast between the P- and S-wave velocities up to the limiting case of an acoustic medium with zero S-wave velocity. By solving a constrained variational problem that makes use of the Lagrange Multiplier method, we develop a mixed formulation that is suitable for implementation in *Hercules*, our finite element code. We illustrate the validity of the method by solving numerically a range of problems, from elastic with moderate contrast of P- to S- wave velocity to the limiting case of an acoustic medium. We also discuss the transition zones formed due to different boundary conditions (*slip, no-slip*) and the change in the wave patterns.

2. Theory

The motion in a linearly elastic continuous system is governed by the equations of elastodynamics (49). Together with the natural, essential and interface boundary conditions given in (50a), (50b) and (50c) we can define the problem presented in Fig. 17 completely.

$$\rho \ddot{u}_i - \sigma_{ij,j} = b_i \tag{49}$$

$$u_i = u_i^* \text{ on } \Gamma_1 \tag{50a}$$

$$\sigma_{ij}\mathbf{n_j} - T_i^* \text{ on } \Gamma_2 \tag{50b}$$

$$(\sigma_{ij}^1 - \sigma_{ij}^2)\mathbf{n_j^*} = 0 \text{ on } \Gamma^* \tag{50c}$$

In these equations, u,ρ,σ,b,$\mathbf{n}$ and T^* are the displacement field, density, stress tensor, body forces, surface normal and the applied traction respectively. Dots stand for time derivatives and the subscript i stand for the component in x_i directon.

Constitutive equations for linear elastic systems are given in (51a), and additionally we define the hydostatic pressure with equation (51b) in terms of bulk and shear moduluses, κ and μ respectively.

$$\sigma_{ij} = \kappa u_{k,k}\delta_{ij} + \mu(u_{i,j} + u_{j,i} - \frac{2}{3}u_{k,k}\delta_{ij}) \tag{51a}$$

$$p = -\kappa u_{k,k} \tag{51b}$$

where δ_{ij} is the Kronecker's delta and subscripts following a comma mean partial derivatives in space with respect to the x_j coordinate.

The mixed finite element method can be formulated using the Galerkin method, in which the constraints are introduced through Lagrange multipliers. Introducing (51b) as the side condition and choosing the pressure as the Lagrange multiplier, we can derive the strong form as given in (52).

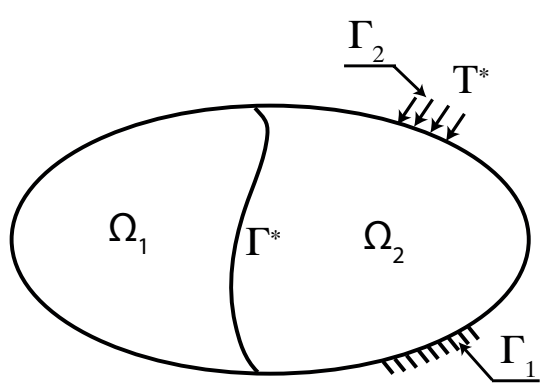

Figure 17: A continuous system

$$
\begin{aligned}
&\int_{\Omega_1\cup\Omega_2} (\rho\ddot{u}_i - \sigma_{ij,j} - b_i)\,\delta u_i d\Omega + \int_{\Gamma_2} (\sigma_{ij}\mathbf{n_j} - T_i^*)\,\delta u_i d\Gamma_2 \\
&+ \int_{\Gamma^*} (\sigma_{ij}^1 - \sigma_{ij}^2)\mathbf{n_j^*} d\Gamma^* + \int_{\Omega_1\cup\Omega_2} \delta p \left(\frac{p}{\kappa} + u_{k,k}\right) d\Omega = 0
\end{aligned}
\tag{52}
$$

Next, we derive the weak form in terms of u and p as given in (53).

$$
\begin{aligned}
&\int_{\Omega_1\cup\Omega_2} \rho\ddot{u}_i \delta u_i d\Omega - \int_{\Omega_1\cup\Omega_2} p\delta u_{i,i} d\Omega \\
&+ \int_{\Omega_1\cup\Omega_2} \left(\frac{1}{2}\mu(u_{i,j} + u_{j,i})(\delta u_{i,j} + \delta u_{j,i}) - \frac{2}{3}\mu u_{k,k}\delta u_{i,i}\delta_{ij}\right) d\Omega \\
&- \int_{\Omega_1\cup\Omega_2} b_i \delta u_i d\Omega - \int_{\Gamma_2} T_i^* \delta u_i d\Gamma_2 \\
&+ \int_{\Omega_1\cup\Omega_2} \delta p(\frac{p}{\kappa} + u_{k,k}) d\Omega = 0
\end{aligned}
\tag{53}
$$

Since we do not have a spatial derivative of the pressure variable p in the weak form, a wider range of interpolation functions are permissible for it including discontinuous functions across element boundaries. Pressure within the elastic material is in general discontinuous not only on the interfaces of different materials but also within the same material. One exception to this is the case of zero shear modulus which corresponds to the acoustic domain. In acoustic domain the traction consists only of pressure, making it continuous. Thus, the choice of discontinuous pressure is more physical.

Spatial discretization through the finite element method with continuous displacement and discontinuous pressure fields, allows one to derive a set of ordinary differential equations as stated in matrix form in (54).

$$
\begin{bmatrix} \mathbf{M}_{uu} & \mathbf{0} \\ \mathbf{0} & \mathbf{0} \end{bmatrix} \begin{bmatrix} \ddot{\mathbf{u}} \\ \ddot{\mathbf{p}} \end{bmatrix} + \begin{bmatrix} \mu\mathbf{K}_{uu} & -\mathbf{K}_{up} \\ -\mathbf{K}_{up}^T & \frac{1}{\kappa}\mathbf{K}_{pp} \end{bmatrix} \begin{bmatrix} \mathbf{u} \\ \mathbf{p} \end{bmatrix} = \begin{bmatrix} \mathbf{f} \\ \mathbf{0} \end{bmatrix}
\tag{54}
$$

A diagonally lumped mass matrix is used to decouple the system of equations with respect to $\mathbf{M}_{uu}$. We use second order central differences to solve (54) step-by-step in time. Thus, the displacements and pressure for any given node i in the mesh, can be evaluated explicitly by (55).

$$
\mathbf{p}_t^{\mathbf{e}} = -(\kappa\mathbf{K}_{pp}^{-1}\mathbf{K}_{up}^T)^{\mathbf{e}}\mathbf{u}_t^{\mathbf{e}} \tag{55a}
$$

$$
\mathbf{u}_{t+1}^i = \frac{\Delta t^2}{m^i}\mathbf{b}_t^i + \left(2\mathbf{u}_t^i - \mathbf{u}_{t-1}^i\right) - \frac{\Delta t^2}{m^i}\sum_e (\mu\mathbf{K}_{uu}^{\mathbf{e}}\mathbf{u}_t^{\mathbf{e}} - \mathbf{K}_{up}^{\mathbf{e}}\mathbf{p}_t^{\mathbf{e}}) \tag{55b}
$$

Here, m_i and b_i are the mass and body force associated with the i-th node of interest while the matrices and the vectors with subscript $\mathbf{e}$ are the local matrices and vectors of the elements associated with node i.

Using discontinuous pressure field allows us to solve (55a) at the element level at each time step. Next, we solve (55b) to get the displacement field for the following time step.

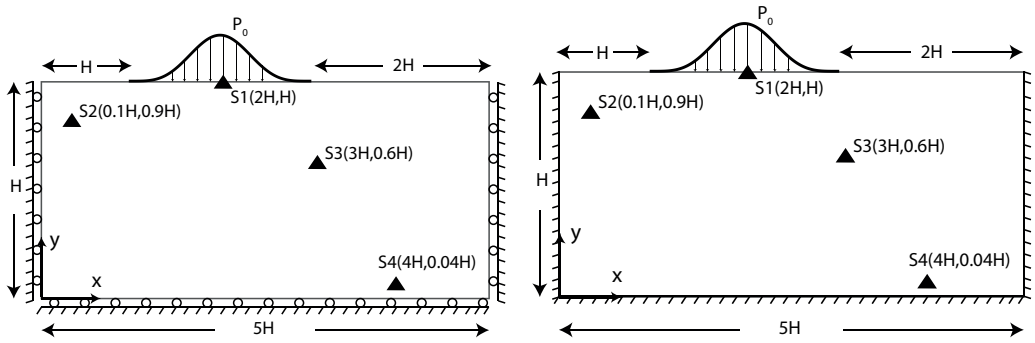

(a) Slip Boundary Condition (b) No-Slip Boundary Conditions

Figure 18: Problem geometry with slip (a) and no-slip (b) boundary conditions. Station locations are marked with triangles and the coordinates are given in terms of 'x' and 'y' where the bottom left corner is taken as the origin.

Although the procedure looks quite straight forward, the stability constraint puts a limitation on the available element types. However, as stated by Bathe (2001) with the correct element types that satisfy the *inf-sup conditon* as introduced by (Babuška, 1971) and (Brezzi, 1974), one can eliminate the *spurious modes* with the mixed formulation. In our examples, we use the *Q2-P1* element, which corresponds to a continuous quadratic displacement field and discontinuous linear pressure field.

Within the limitations of linear elasticity, we can model any material extending from elastic to acoustic by changing shear and bulk moduli. In the extreme case of an acoustic medium, the shear modulus becomes zero. In this case the stiffness matrix $\mu \mathrm{K}_{uu}$ in (54) vanishes.

3. Numerical Results

3.1. Problem Definition and Simulation Parameters

We have implemented and tested the methodology described in Chapter **??** by way of several specific two-dimensional. These problems can be grouped into two categories with different boundary conditions, slip and no-slip, on three sides (left, right and bottom) and free at the top with a normal traction acting on it as shown in Fig. 18.

These problems with the acoustic domain characteristics (zero S-wave velocity) can be considered as extreme cases of fluid-structure interaction problems (rigid and frictionless solid-fluid interaction) where the two different models (slip and no slip) are tested and compared using the same mixed finite element formulation.

To observe the differences that occur over the transition from elastic to acoustic medium, we consider four different S- to P-wave velocity ratios, ranging from a moderate value (0.5) to extreme (0). For the intermediate cases we also considered the ratios $\mathrm{V_s}/\mathrm{V_p} = 0.1, 0.01$.

We used the same mesh for all the simulations as defined in Table 1. Using rectangular elements, higher resolution is achieved in the horizontal direction compared to the vertical one. This is done so primarily

Table 1: Mesh and simulation parameters in terms of normalized values for the problems worked on.

Mesh Properties	
Element Dimensions	
h_x	0.005H
h_y	0.02H
Number of Elements	
N	$50,000$

Simulation Characteristics	
V_s/V_p	0, 0.01, 0.1, 0.5
$\bar{f}_{max}$	5 (See 19(b))
Time step($\bar{dt}$)	6.25×10^{-4}
Simulation Time($\bar{T}$)	30

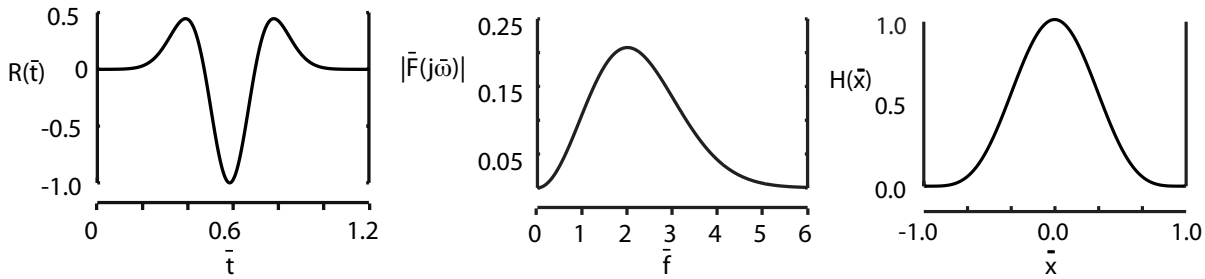

(a) Time History - Ricker Pulse (b) Fourier Transform (c) Spatial Distribution

Figure 19: Time history (a), spatial distribution (b) and the Fourier transform (c) of the normal traction applied on the surface in terms of normalized values where the normalized frequency $\bar{f} = \frac{fH}{V_p}$.

to observe more clearly the shear wave propagation and the transition zone that forms close to vertical boundaries. Tests with coarser and refined meshes with both rectangular and square elements justify the choice of this particular mesh.

The governing equations of the problem and the constraint introduced in the methodology as described in Chap. **??** are normalized as given in (56a) and (56b).

$$\frac{\partial^2 \bar{u}_i}{\partial \bar{t}^2} = -\frac{\partial \bar{p}}{\partial \bar{x}_i} + \left(\frac{V_s}{V_p}\right)^2 \sum_j \frac{\partial^2 \bar{u}_i}{\partial \bar{x}_j^2} + \bar{b}_i \tag{56a}$$

$$\bar{p} = -\left[\left(\frac{V_p}{V_s}\right)^2 - 1\right] \sum_k \frac{\partial \bar{u}_k}{\partial \bar{x}_k} \tag{56b}$$

where $\bar{x}_i = \frac{x_i}{H}$, $\bar{t} = \frac{tV_p}{H}$, $\bar{u}_i = \frac{u_i \rho V_p^2}{p_0 H}$, $\bar{p} = \frac{p}{p_0}$ and $\bar{b}_i = \frac{b_i H}{V_p}$ are the normalized variables corresponding to spatial variable, time, displacement component, pressure and body force component respectively. Since we do not have any body forces, the b_i components are zero.

For the problems studied, the normal traction acting on the free surface is given in (57) and Fig. 19.

$$p(\bar{x}, \bar{t}) = p_0 R(\bar{t}) H(\bar{x}) \tag{57a}$$

$$\mathrm{H}(\bar{\mathrm{x}}) = \frac{1}{4}\left[1 + \cos\left(\frac{\pi\bar{x}}{H}\right)\right]^2 \tag{57b}$$

Here, $\mathrm{R}(\bar{\mathrm{t}})$ is the Ricker Pulse, whose definition can be found in Ricker and Sorge (1951) or Bamberger and Tran (1991).

3.2. Results of the Simulation

Figure 20 shows the absolute peak velocity over the domain, for different boundary conditions and material properties. Comparing the first and the second rows corresponding to no-slip and slip condition problems respectively, one can clearly see the effect of the boundary on the peak velocity values. This effect decreases in size as we decrease the S- and P-wave velocity ratio, reducing the shear effect in the material. This effect is confined to the surrounding boundaries. The propagation of the transition zone becomes more evident by comparing Figure 21 with Figure 22, where we present snapshots of the absolute velocity values during the simulations. The transition zone moves into the domain with decreasing velocity as we decrease the S- to P-wave velocity ratio. For the rest of the domain, the results for slip and no-slip boundary conditions essentially match each other.

The peak pressure values and the snapshots of the absolute pressure values are shown in Figures 23, 24 and 25. The transition zones formed due to the boundary conditions clearly affect the pressure values. This effect decreases just like the transition zone size as the shear effect decreases.

The transition from elastic to acoustic case raises the question of how similar the results are for different values of $\mathrm{V_s}/\mathrm{V_p}$. For the problems studied with no-slip boundary conditions, we have observed that the shear effect is visible even for the S- and P-wave ratio of 0.1 which can be considered as a clay material. Nevertheless, the difference between a ratio of 0.01 and the fully acoustic case is negligible.

For the slip-boundary condition problems, we can include the ratio of 0.1 to the class of materials for which the results change only slightly with respect to the acoustic case.

To have a closer look at the points in the vicinity of the boundaries and away from them, we show the components of velocity and pressure at various stations, in Figures 26 through 29. See Figure 18 for station locations.

Station S1 is located directly under the loaded area. Its pressure output gives a clear idea about how similar the material is to an acoustic case. The normal traction must be equal to the pressure for the acoustic problem but not for the other cases. The similarity of the pressure to the applied traction serves to asses the differences in the behavior.

For stations S2 and S4 located in the vicinity of the boundaries, the horizontal component of velocity best illustrates the transition zone, which decreases as $\mathrm{V_s}/\mathrm{V_p}$ gets smaller.

Finally, the station S3 located away from the boundaries is chosen to observe the behavior within the domain. The arrival at this station of the waves generated at the no slip boundaries can clearly be seen from the comparison of the no-slip and slip boundary condition problems.

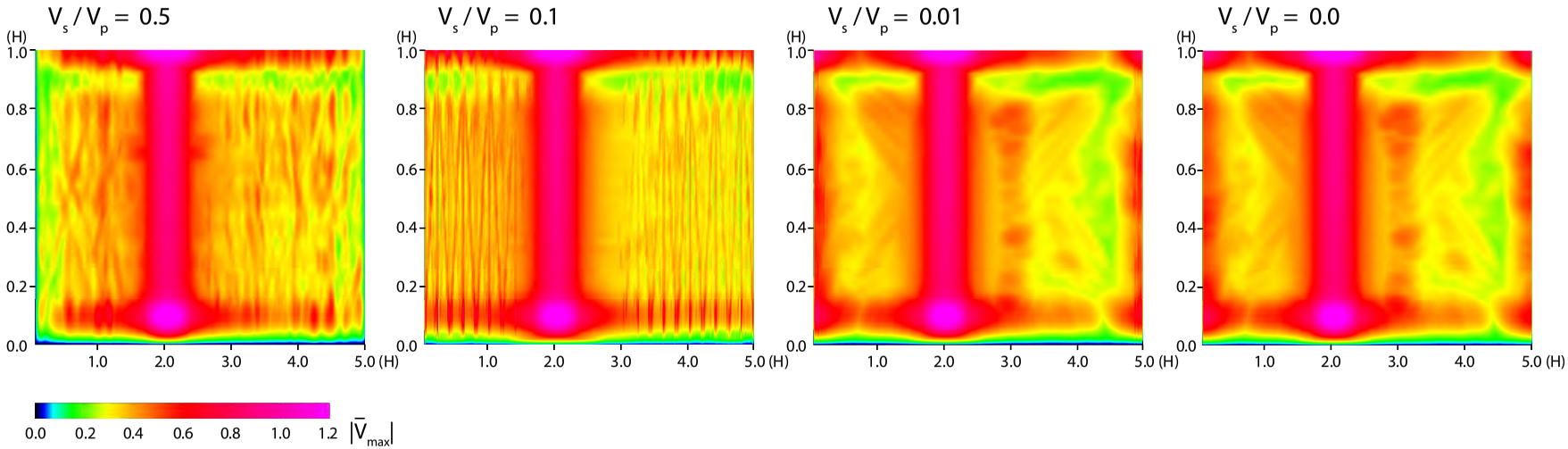

(a) No-Slip Boundary Conditions

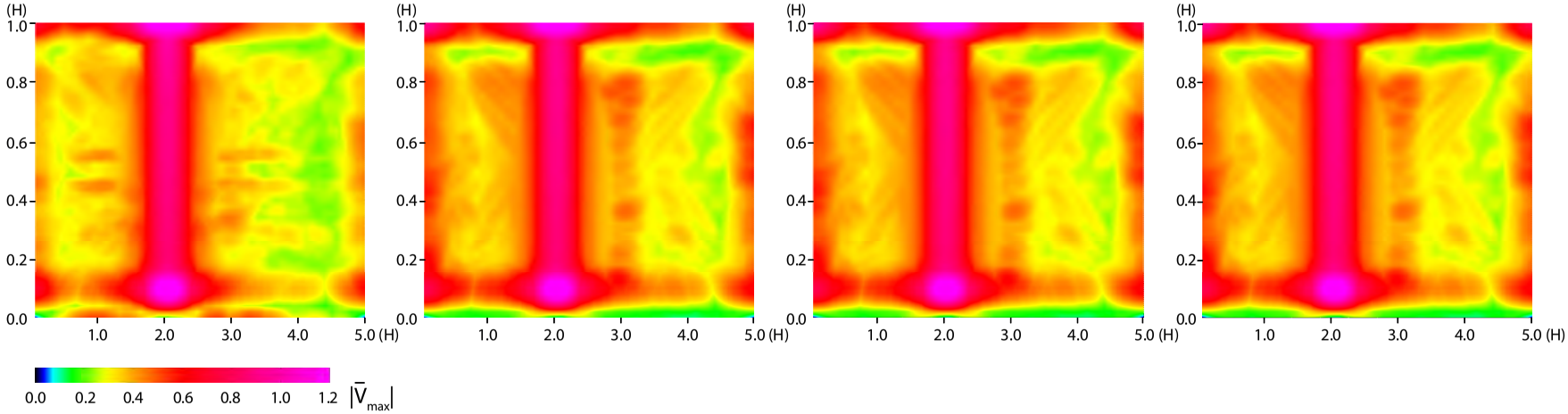

(b) Slip Boundary Conditions

Figure 20: Normalized absolute peak velocities on the plane during the whole simulations with no-slip boundary conditions (a) and slip boundary conditions (b) for different S- and P-wave velocity ratios.

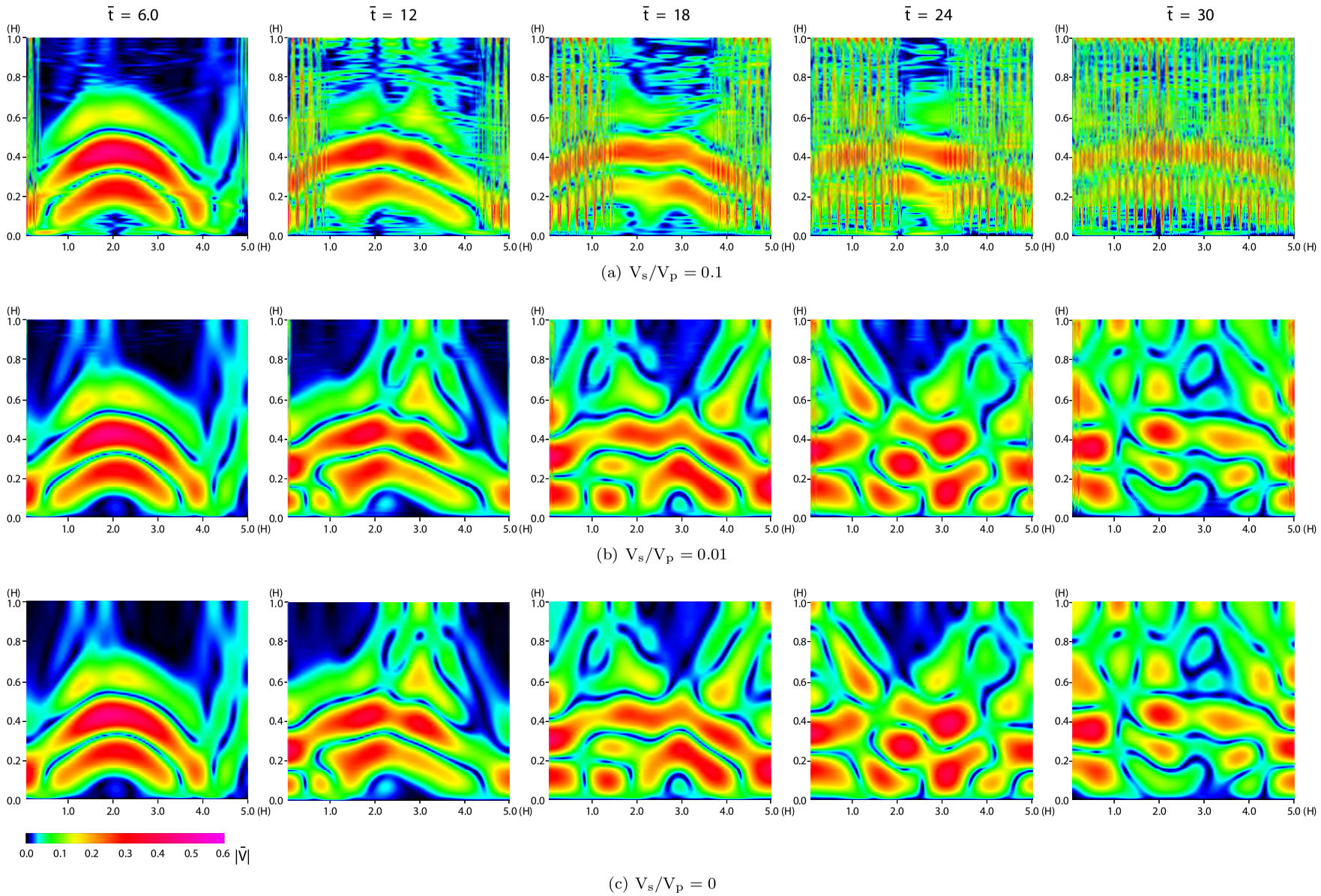

Figure 21: Snapshots of the absolute velocity during the simulation for the problem with different material properties and no-slip boundary conditions, $V_s/V_p = 0.1$ (a), $V_s/V_p = 0.01$ (b) and $V_s/V_p = 0$ (c).

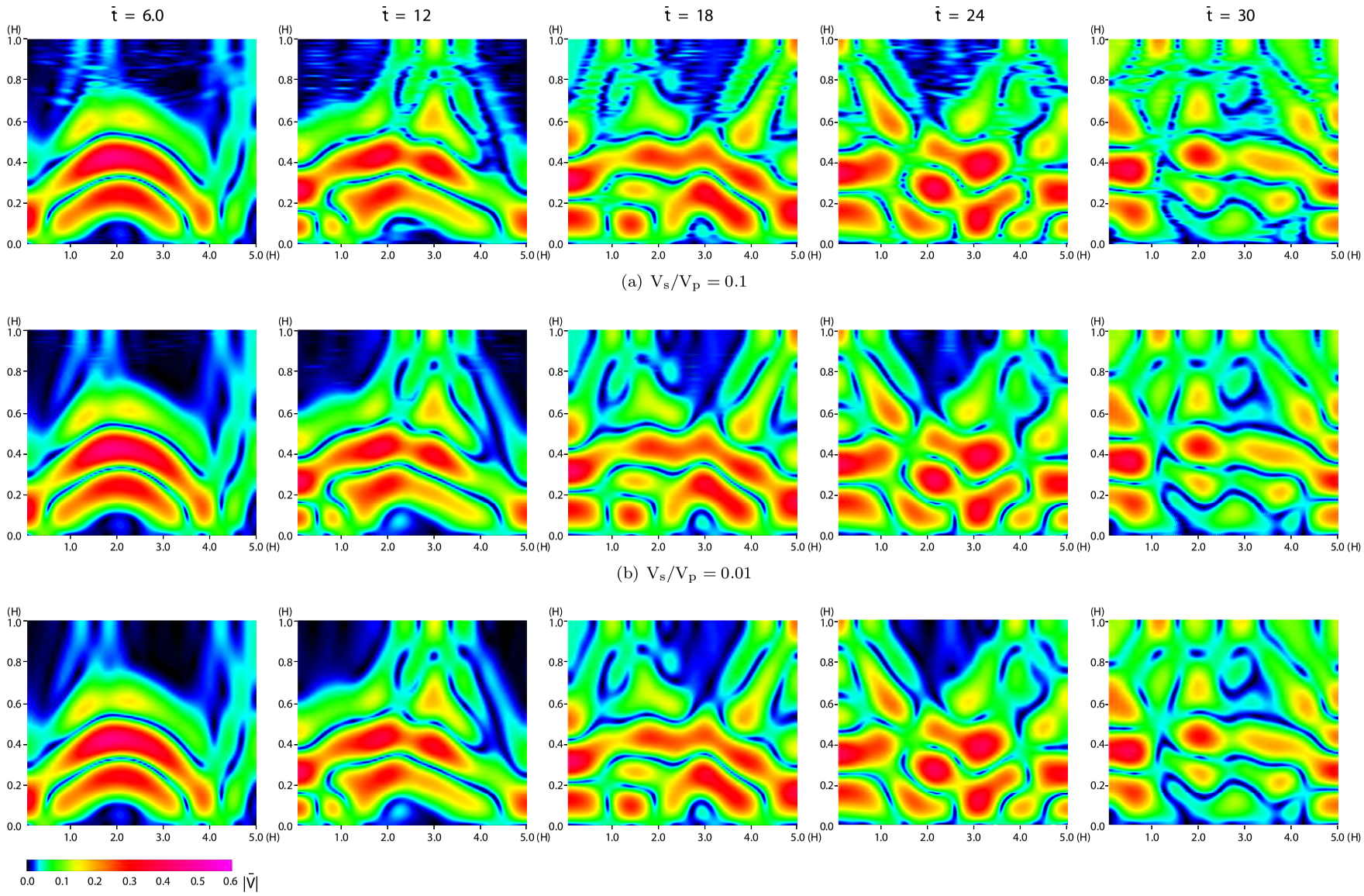

(a) $V_s/V_p = 0.1$

(b) $V_s/V_p = 0.01$

(c) $V_s/V_p = 0$

Figure 22: Snapshots of the absolute velocity during the simulation for the problem with different material properties and slip boundary conditions, $V_s/V_p = 0.1$ (a), $V_s/V_p = 0.01$ (b) and $V_s/V_p = 0$ (c).

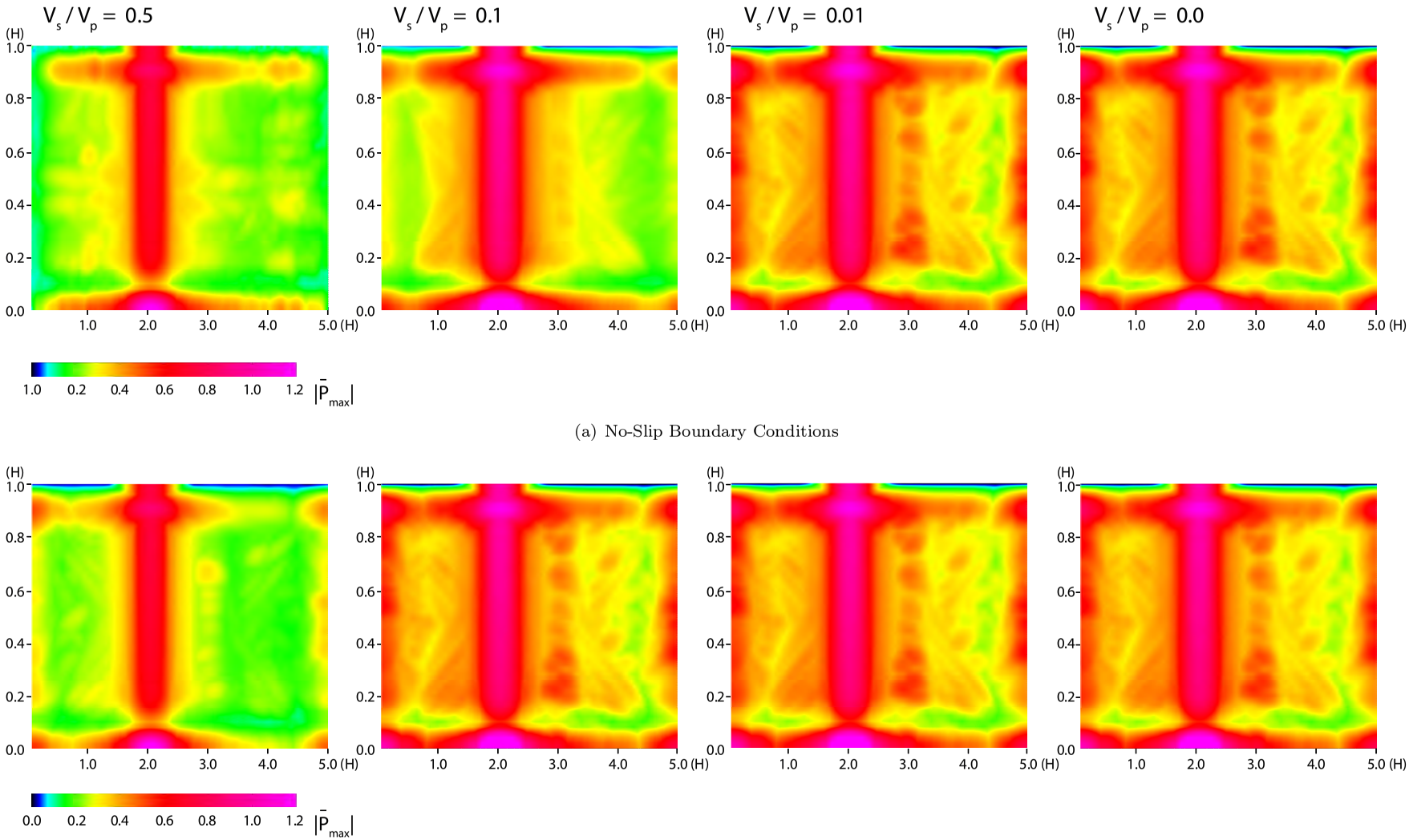

(a) No-Slip Boundary Conditions

(b) Slip Boundary Conditions

Figure 23: Normalized absolute peak pressures on the plane during the whole simulations with no-slip boundary conditions (a) and slip boundary conditions (b) for different S- and P-wave velocity ratios.

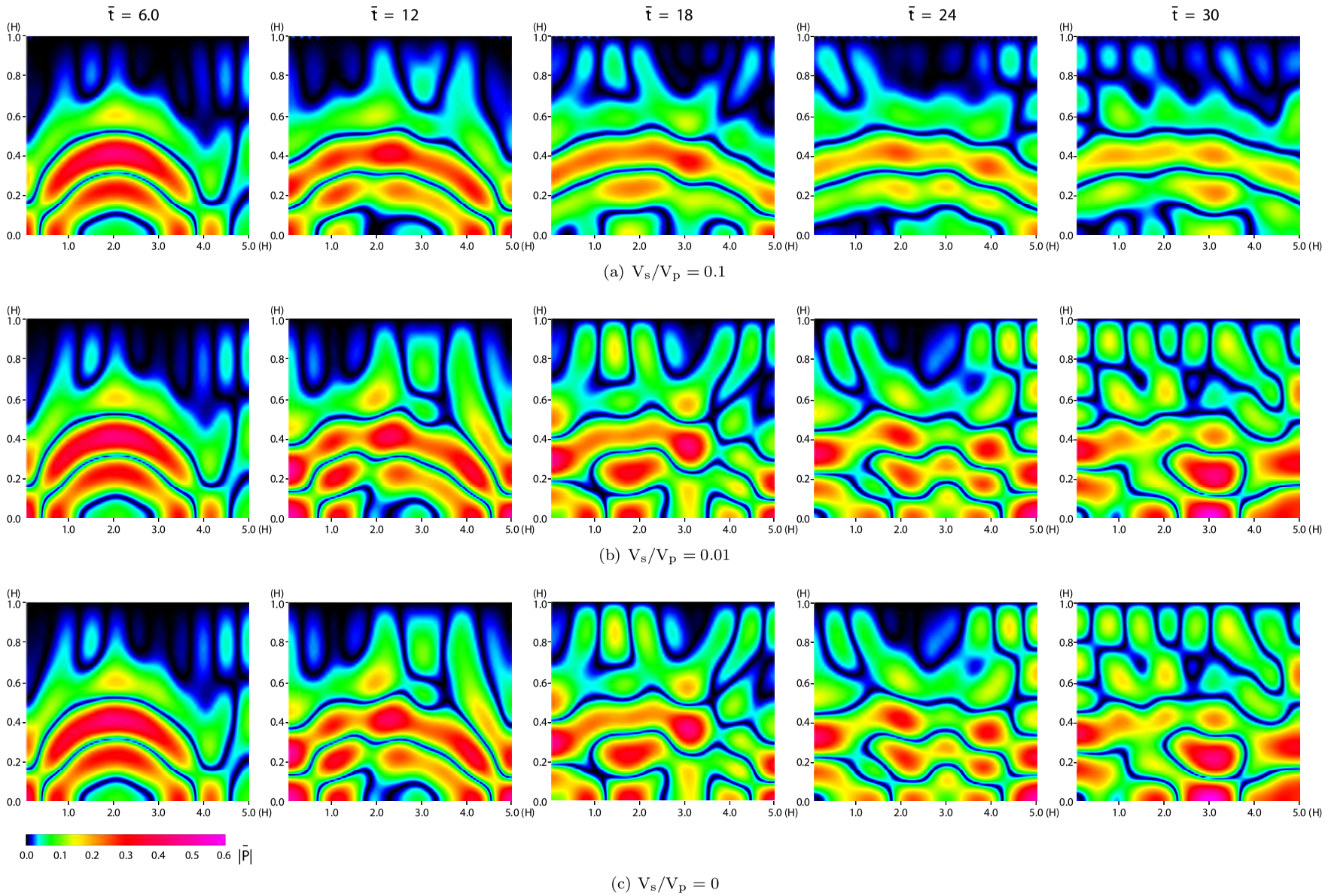

Figure 24: Snapshots of the absolute pressure during the simulation for the problem with different material properties and no-slip boundary conditions, $V_s/V_p = 0.1$ (a), $V_s/V_p = 0.01$ (b) and $V_s/V_p = 0$ (c).

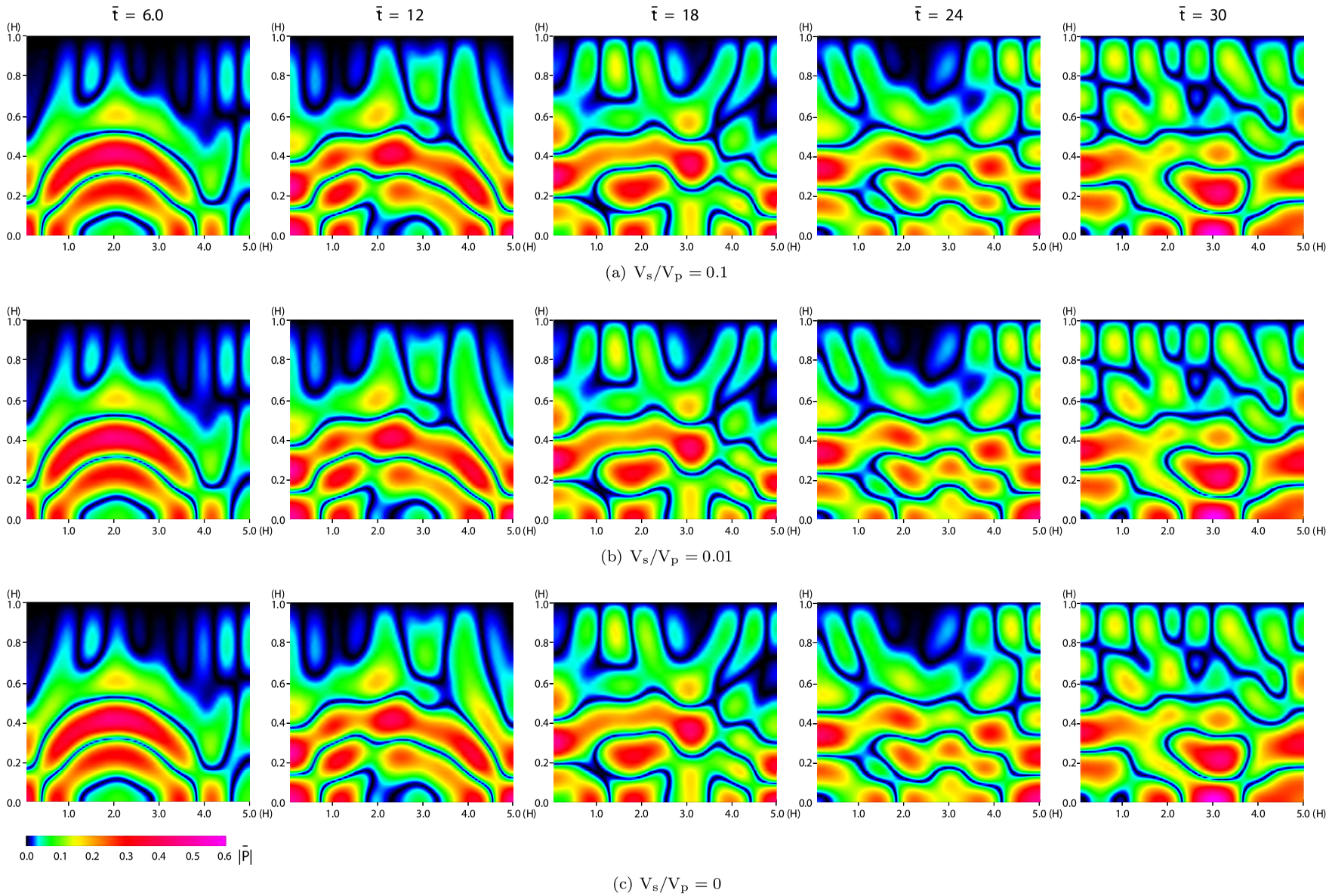

Figure 25: Snapshots of the absolute pressure during the simulation for the problem with different material properties and slip boundary conditions, $V_s/V_p = 0.1$ (a), $V_s/V_p = 0.01$ (b) and $V_s/V_p = 0$ (c).

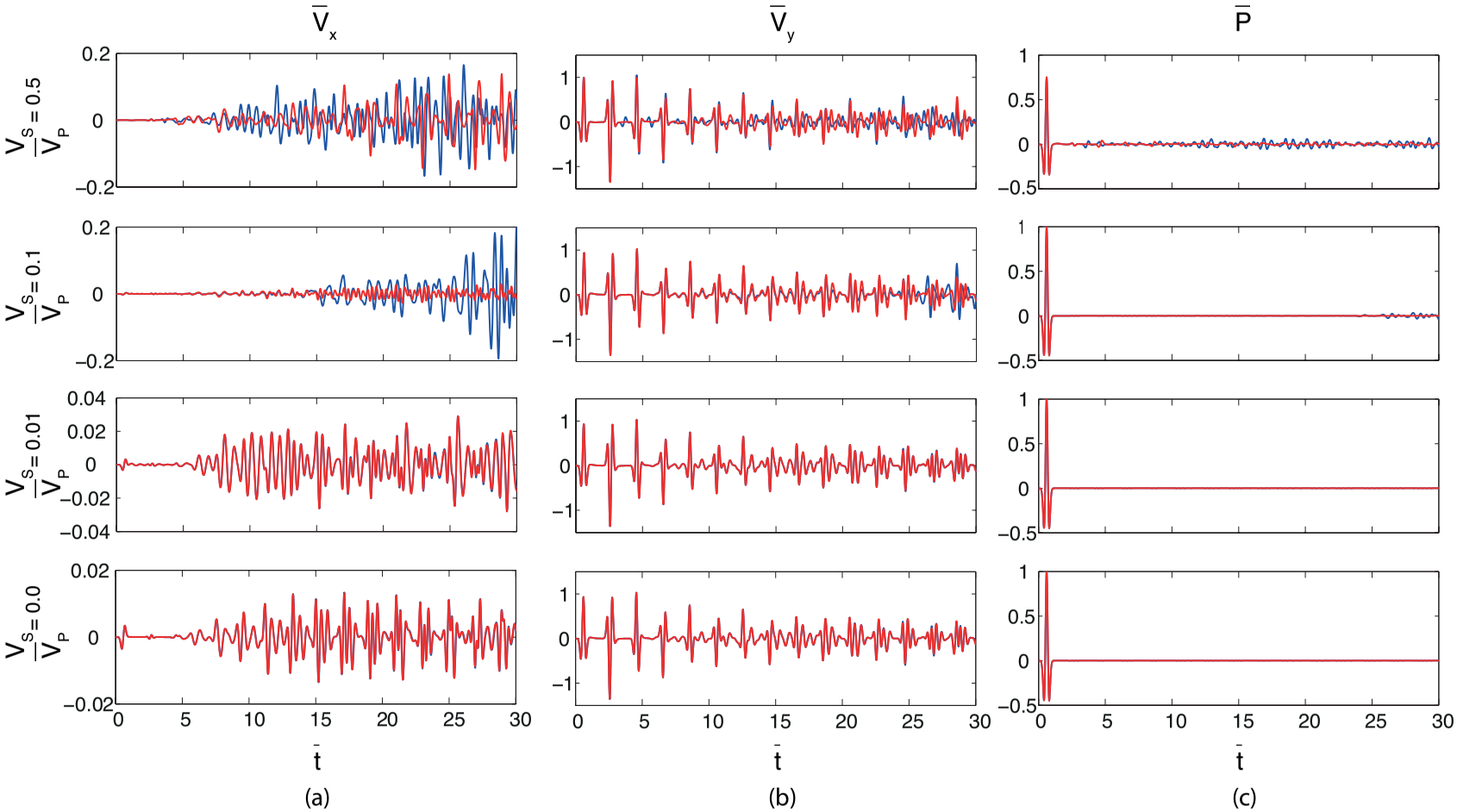

Figure 26: Comparison of the normalized velocity components ($\bar{V}_x$, $\bar{V}_y$ (b)) and pressure (c) at station S1 between the problems with no-slip (blue) and slip (red) boundary conditions.

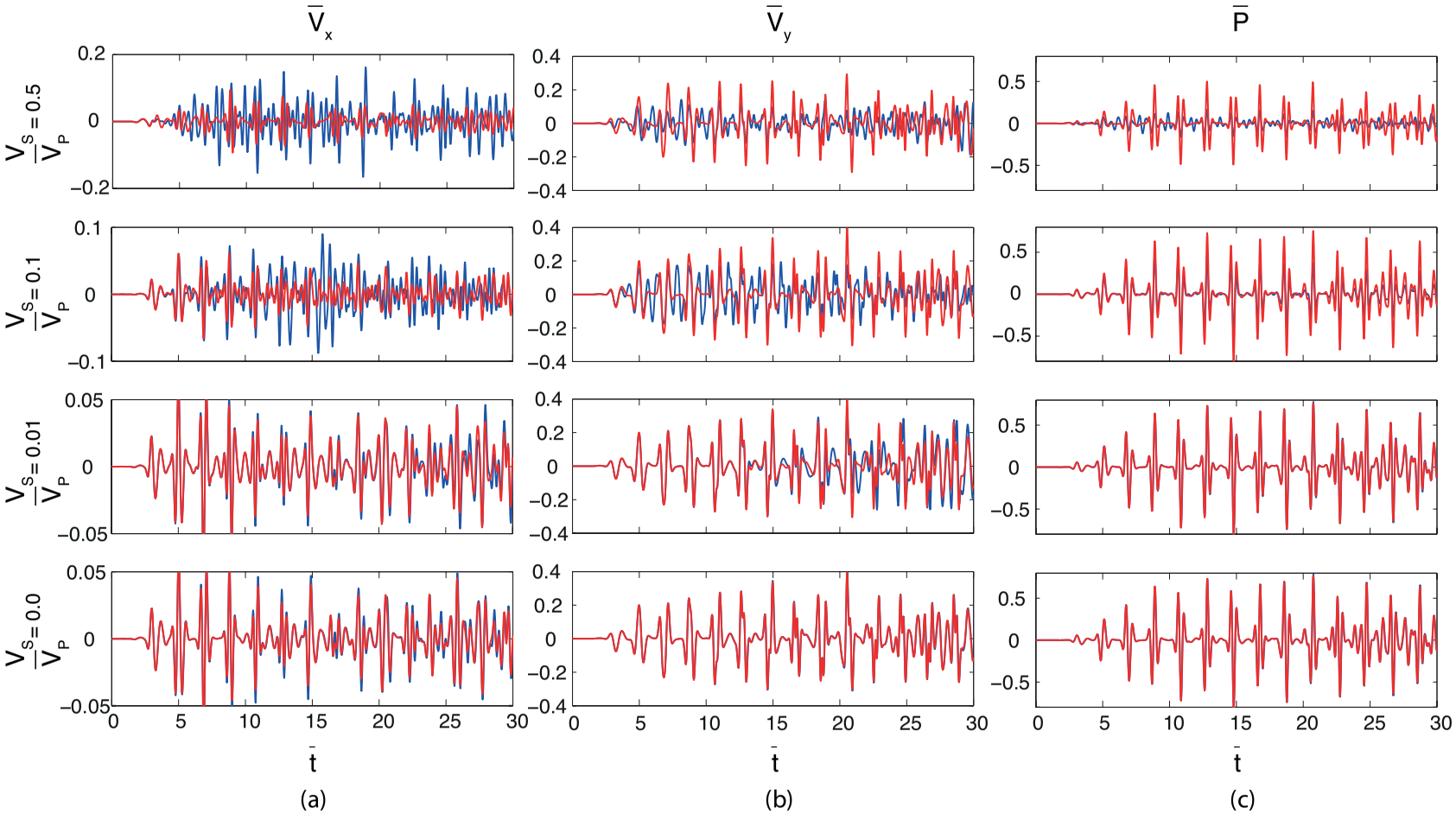

Figure 27: Comparison of the normalized velocity components ($\bar{V}_x$, $\bar{V}_y$ (b)) and pressure (c) at station S2 between the problems with no-slip (blue) and slip (red) boundary conditions.

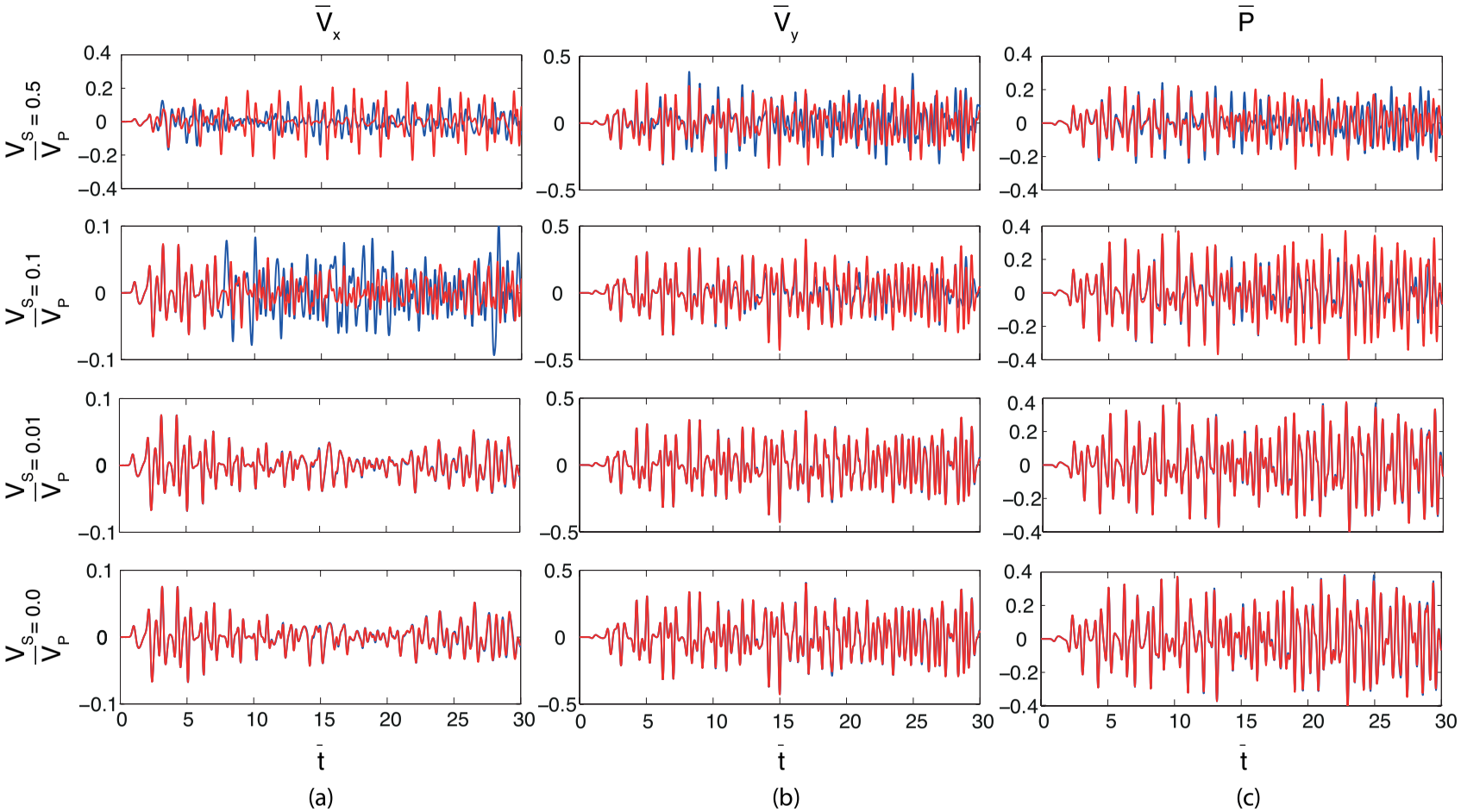

Figure 28: Comparison of the normalized velocity components ($\bar{V}_x$, $\bar{V}_y$ (b)) and pressure (c) at station S3 between the problems with no-slip (blue) and slip (red) boundary conditions.

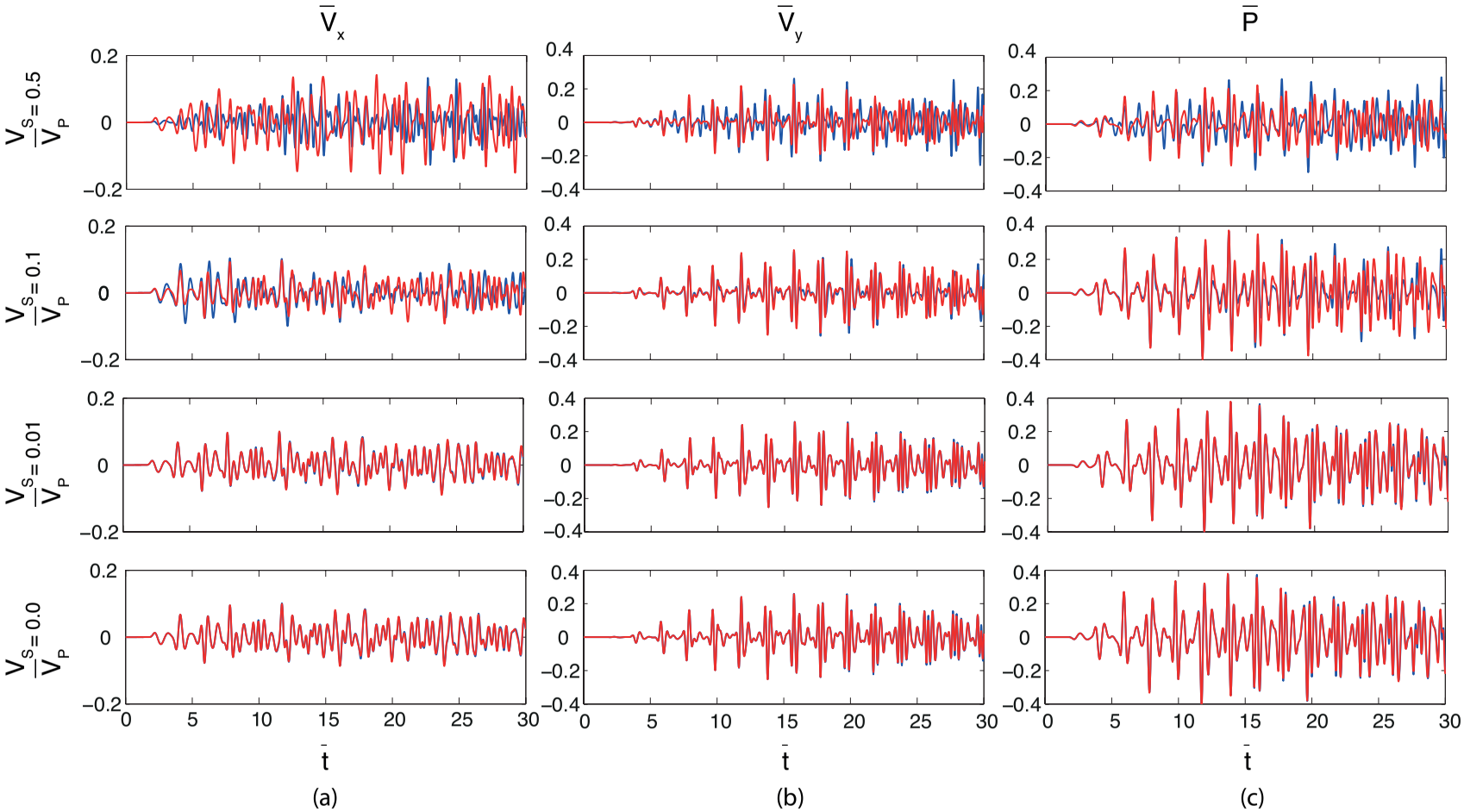

Figure 29: Comparison of the normalized velocity components ($\bar{V}_x$, $\bar{V}_y$ (b)) and pressure (c) at station S4 between the problems with no-slip (blue) and slip (red) boundary conditions.

4. Conclusions

We modeled materials that range from elastic with moderate S- and P-wave velocity ratio to acoustic with zero S-wave velocity (no shear). We implemented a mixed finite element formulation with displacement and pressure as the primary variables to overcome the limitations of the displacement-based formulations.

We tested this unifying approach and the numerical method on two-dimensional dynamic problems. We also compared different boundary conditions, namely, no-slip and slip boundary conditions. This is considered as critical, since the mixed method allows displacement-based boundary conditions to be imposed. This is not possible in a pressure-based formulation, as commonly used for acoustic media.

Since the displacements should be continuous across the fluid-solid interfaces even if the shear modulus is extremely small, we focus on problems with no-slip condition. These tests represent solid-fluid interaction problems where the fixed boundaries can be considered as a rigid solid and tangentially free-ones as a frictionless solid.

References

Aagaard, B. T., Brocher, T. M., Dolenc, D., Dreger, D., Graves, R. W., Harmsen, S., Hartzell, S., Larsen, S., and Zoback, M. L. (2008). Ground-motion modeling of the 1906 san francisco earthquake, part i: Validation using the 1989 loma prieta earthquake. *Bull. Seism. Soc. Am.*, 98(2):989–1011.

Anandarajah, A. (2010). *The DruckerPrager Model and Its Integration, in Computational Methods in Elasticity and Plasticity*, chapter 13, pages 513–560. Springer New York.

Babuška, I. (1971). Error-bounds for finite element method. *Numerische Mathematik*, 16(4):322–333.

Bamberger, A. and Tran, Q. (1991). Propagation and attenuation of a ricker pulse in one-dimensional randomly heterogeneous media: a numerical study. In *Proceedings of the 10th international conference on computing methods in applied sciences and engineering on Computing methods in applied sciences and engineering*, pages 217–247. Nova Science Publishers, Inc.

Bathe, K. (2001). The inf–sup condition and its evaluation for mixed finite element methods. *Computers & Structures*, 79(2):243–252.

Beresnev, I. A., Field, E. H., Van Den Abeele, K., and Johnson, P. A. (1998). Magnitude of nonlinear sediment response in los angeles basin during the 1994 northridge, california, earthquake. *Bull. Seism. Soc. Am.*, 88(4):1079–1084.

Bićanić, N. and Pearce, C. J. (1996). Computational aspects of a softening plasticity model for plain concrete. *Mechanics of Cohesive-frictional Materials*, 1(1):75–94.

Borja, R. I. and Lee, S. R. (1990). Cam-clay plasticity, part 1: Implicit integration of elasto-plastic constitutive relations. *Computer Methods in Applied Mechanics and Engineering*, 78(1):49 – 72.

Brezzi, F. (1974). On the existence, uniqueness and approximation of saddle-point problems arising from lagrangian multipliers. *RAIRO Anal. Numer*, 8(2):129–151.

Chen, W.-F. and Mizuno, E. (1990). *Nonlinear analysis in soil mechanics: theory and implementation.* Amsterdam: Elsevier.

de Souza Neto, E. A., Perić, D., and Owen, D. R. J. (2008). *The mathematical Theory of Plasticity, in Computational Methods for Plasticity: Theory and Applications*, chapter 6, pages 137–190. John Wiley & Sons, Ltd.

Drucker, D. C. and Prager, W. (1952). Soil mechanics and plastic analysis or limit design. *Quarterly of Applied Mathematics*, 10:157–164.

Elgamal, A.-W. (1991). Shear hysteretic elasto-plastic earthquake response of soil systems. *Earthquake Engineering & Structural Dynamics*, 20(4):371–387.

Fabrice, D., Florent, D. M., Evelyne, F., Dimitri, K., and Jean, R. (2010). High-performance finite-element simulations of seismic wave propagation in three-dimensional nonlinear inelastic geological media. *Parallel Computing*, 36:308 – 325.

Field, E. H. and the SCEC Phase III Working Group (2000). Accounting for site effects in probabilistic seismic hazard analyses of southern california: Overview of the scec phase iii report. *Bull. Seism. Soc. Am.*, 90(6B):S1–S31.

Graves, R. W. and Pitarka, A. (2010). Broadband ground-motion simulation using a hybrid approach. *Bull. Seism. Soc. Am.*, 100(5A):2095–2123.

Graves, R. W., Pitarka, A., and Somerville, P. G. (1998). Ground-motion amplification in the santa monica area: Effects of shallow basin-edge structures. *Bull. Seism. Soc. Am.*, 88(5):1224–1242.

Hamdi, M., Ousset, Y., and Verchery, G. (1978). A displacement method for the analysis of vibrations of coupled fluid-structure systems. *International Journal for Numerical Methods in Engineering*, 13(1):139–150.

Hartzell, S., Bonilla, L. F., and Williams, R. A. (2004). Prediction of nonlinear soil effects. *Bull. Seism. Soc. Am.*, 94(5):1609–1629.

Hughes, T. (2000). *The finite element method: linear static and dynamic finite element analysis*, volume 65. Dover Publications.

Idriss, I. M. and Seed, H. B. (1968). An analysis of ground motions during the 1957 san francisco earthquake. *Bull. Seism. Soc. Am.*, 58(6):2013–2032.

Iwan, W. D. (1967). On a class of models for the yielding behavior of continuous and composite systems. *Journal of Applied Mechanics*, 34(3):612–617.

Joyner, W. B. (1975). A method for calculating nonlinear seismic response in two dimensions. *Bull. Seism. Soc. Am.*, 65(5):1337–1357.

Joyner, W. B. and Chen, A. T. F. (1975). Calculation of nonlinear ground response in earthquakes. *Bull. Seism. Soc. Am.*, 65(5):1315–1336.

Kiefling, L. and Feng, G. (1976). Fluid-structure finite element vibrational analysis. *AIAA Journal*, 14:199–203.

Kramer, S. L. (1996). *Geotechnical Earthquake Engineering*. Prentice Hall.

Marsh, J., Larkin, T. J., Haines, A. J., and Benites, R. A. (1995). Comparison of linear and nonlinear seismic responses of two-dimensional alluvial basins. *Bull. Seism. Soc. Am.*, 85(3):874–889.

Olson, L. and Bathe, K. (1983). A study of displacement-based fluid finite elements for calculating frequencies of fluid and fluid-structure systems. *Nuclear Engineering and Design*, 76(2):137–151.

Perzyna, P. (1963). The constitutive equations for rate sensitive plastic materials. *Quarterly of Applied Mathematics*, 20:321–332.

Prandtl, L. (1904). Motion of fluids with very little viscosity. In *Proceedings of 3rd International Mathematics Congress Heidelberg*.

Restrepo, D., Taborda, R., and Bielak, J. (2011). Effects of soil nonlinearity on ground response in 3d simulations – an application to the salt lake city basin. *Proceedings of the 4th IASPEI/IAEE International Symposium: Effects of Surface Geology on Seismic Motion, University of California, Santa Barbara, August 23-26*.

Ricker, N. and Sorge, W. (1951). The primary seismic disturbance in shale. *Bulletin of the Seismological Society of America*, 41(3):191–204.

Simo, J. and Hughes, T. (1998). *Computational Inelasticity Interdisciplinary Applied Mathematics 7*. Springer-New York.

Taborda, R. (2010). *Three Dimensional Nonlinear Soil and Site-City Effects in Urban Regions*. PhD thesis, Carnegie Institute of Technology, Carnegie Mellon University, Pittsburgh, PA.

Taborda, R. and Bielak, J. (2011). Large-scale earthquake simulation: Computational seismology and complex engineering systems. *Computing in Science and Engg.*, 13(4):14–27.

Wald, D. J., Heaton, T. H., and Hudnut, K. W. (1996). The slip history of the 1994 northridge, california, earthquake determined from strong-motion, teleseismic, gps, and leveling data. *Bull. Seism. Soc. Am.*, 86(1B):S49–S70.

Xu, J., Bielak, J., Ghattas, O., and Wang, J. (2003). Three-dimensional nonlinear seismic ground motion modeling in basins. *Physics of the Earth and Planetary Interiors*, 137:81 – 95.

Yu, H.-S. (2006). *Plasticity and Geotechnics*. Springer.

Zhang, Y., Conte, J. P., Yang, Z., Elgamal, A., Bielak, J., and Acero, G. (2008). Two-dimensional nonlinear earthquake response analysis of a bridge-foundation-ground system. *Earthquake Spectra*, 24(2):343–386.

Zienkiewicz, O. and Newton, R. (1969). *Coupled vibrations of a structure submerged in a compressible fluid*.